NEUROSCIENCE

Frontal noradrenergic and cholinergic transients exhibit distinct spatiotemporal dynamics during competitive decision-making

Hongli Wang[1]†, Heather K. Ortega[1]†, Emma B. Kelly[2,3], Jonathan Indajang[3], Neil K. Savalia[1,3,4], Samira Glaeser-Khan[2], Jiesi Feng[5], Yulong Li[5,6,7,8], Alfred P. Kaye[2,9,10], Alex C. Kwan[2,3,11]*

Norepinephrine (NE) and acetylcholine (ACh) are crucial for learning and decision-making. In the cortex, NE and ACh are released transiently at specific sites along neuromodulatory axons, but how the spatiotemporal patterns of NE and ACh signaling link to behavioral events is unknown. Here, we use two-photon microscopy to visualize neuromodulatory signals in the premotor cortex (medial M2) as mice engage in a competitive matching pennies game. Spatially, NE signals are more segregated with choice and outcome encoded at distinct locations, whereas ACh signals can multiplex and reflect different behavioral correlates at the same site. Temporally, task-driven NE transients were more synchronized and peaked earlier than ACh transients. To test functional relevance, we stimulated neuromodulatory signals using optogenetics to find that NE, but not ACh, increases the animals' propensity to explore alternate options. Together, the results reveal distinct subcellular spatiotemporal patterns of ACh and NE transients during decision-making in mice.

INTRODUCTION

Neuromodulators including acetylcholine (ACh) and norepinephrine (NE) play pivotal roles in various behavioral functions (*1*–*3*). One function associated with central cholinergic tone is arousal and vigilance (*4*), which relate to sensory sensitivity and selective attention (*5*, *6*). These functions are supported by many experiments that manipulated cholinergic signaling using pharmacology, lesions, and optogenetics (*7*–*12*). Classically, perceptual effects are associated with slow fluctuation of ACh levels, although recent evidence indicates control can also occur at more rapid timing (*10*, *13*, *14*). Relatedly, NE has also been implicated in arousal and vigilance (*15*, *16*), and improved sensitivity to sensory cues (*17*). This is possibly achieved by NE elevating the signal-to-noise ratio and/or gain in neural networks (*18*, *19*). The neuromodulatory effects on behavior, such as those exerted by NE, exhibit an inverted U-shaped curve (*20*). Activity of cortical cholinergic and noradrenergic axons correlates well with pupil diameter, which is an indicator of the arousal level of an animal (*21*).

In addition to arousal and vigilance, it is established that ACh and NE may be important for learning and decision-making (*22*–*27*). For instance, cholinergic neurons in the basal forebrain exhibit fast and transient increase in spiking activity after primary reinforcements including rewards and punishments (*28*, *29*). In support, optogenetic activation of cortical cholinergic axons could substitute for actual rewards in associative learning (*30*). Memory deficits have been observed when cholinergic transmission was abolished in animals (*11*, *31*). NE may be similarly crucial for learning and decision-making because a loss of adrenergic receptors in the prefrontal cortex contributes to the memory loss in aged animals (*32*, *33*). More specifically, locus coeruleus (LC) neurons fire at specific epochs during decision tasks (*34*) and may be sensitive to reward values (*35*). These firing changes in cholinergic or noradrenergic nuclei likely lead to altered phasic release of neuromodulators that have been observed in the cortex (*36*). Therefore, growing evidence indicate functions of ACh and NE signaling in higher cognitive functions.

The neuromodulatory ACh and NE signals come from different sources and have distinct projection patterns. The main source of ACh in the neocortex comes from the basal forebrain. The axonal projections are organized topographically (*37*–*39*) and exhibit rich spatiotemporal dynamics across regions (*40*). By contrast, a major source of NE is LC, which sends axons to innervate much of the forebrain, although with some exceptions, such as the basal ganglia (*41*, *42*). Each LC neuron projects broadly to many brain regions (*43*, *44*) with a high divergence of >20,000 terminals (*45*), although emerging evidence has indicated modularity in efferent projection patterns and function emanating from subpopulations of LC neurons (*46*, *47*).

Despite the large body of literature showing that ACh and NE are associated with multiple behavioral functions, act at multiple timescales, and arise from distinct sources, less is known about the fine spatial pattern of the neuromodulatory signal at micrometer-scale resolution within a cortical region. We know that ACh and NE concentrations must vary in space at the subcellular scale (*48*–*52*). This is because the neuromodulators are released at their respective axonal fiber terminals. Levels of ACh and NE would be highest transiently after release at the terminals and then diffuse, and the concentration falls precipitously as a function of distance. The spatial extent of the signaling is localized further due to expression of proteins such as acetylcholinesterase that quickly eliminate the neuromodulators in

[1]Interdepartmental Neuroscience Program, Yale University School of Medicine, New Haven, CT 06511, USA. [2]Department of Psychiatry, Yale University School of Medicine, New Haven, CT 06511, USA. [3]Meinig School of Biomedical Engineering, Cornell University, Ithaca, NY 14853, USA. [4]Medical Scientist Training Program, Yale University School of Medicine, New Haven, CT 06511, USA. [5]State Key Laboratory of Membrane Biology, Peking University School of Life Sciences, Beijing, China. [6]PKU-IDG/McGovern Institute for Brain Research, Beijing, China. [7]Peking-Tsinghua Center for Life Sciences, Academy for Advanced Interdisciplinary Studies, Peking University, Beijing, China. [8]Chinese Institute for Brain Research, Beijing, China. [9]VA National Center for PTSD Clinical Neuroscience Division, West Haven, CT 06477, USA. [10]Wu Tsai Institute, New Haven, CT 06511, USA. [11]Department of Psychiatry, Weill Cornell Medicine, New York, NY 10065, USA.
*Corresponding author. Email: alex.kwan@cornell.edu
†These authors contributed equally to the work.

extracellular space. We also know that this micrometer-scale spatial distribution of local hotspots of ACh and NE transients in space is likely crucial to the function of cortical microcircuits because the neuromodulators influence subcellular compartments via short- and long-term synaptic plasticity (*53*–*55*). However, the fine spatial patterns for ACh and NE signaling in vivo, particularly during behavior, are unclear. For these reasons, we hypothesize that the spatiotemporal dynamics of the localized ACh and NE signaling in the frontal cortex may relate to decision-related variables to facilitate reinforcement learning during decision-making.

In this study, we test the hypothesis by leveraging the latest generation of genetically encoded fluorescent indicators of ACh (*56*) and NE (*57*, *58*), which permit sensitive and spatially resolved imaging of neuromodulatory signals. We trained head-fixed mice to play a competitive game called matching pennies against a computer opponent (*59*). The matching pennies game requires reward-based learning and has been used extensively to study the role of the frontal cortex in decision-making (*60*–*63*). In the mouse secondary motor cortex (medial M2, the dorsal most aspect of the medial frontal cortex), we found that, although both NE and ACh transients encoded the same set of task-related variables on a trial-by-trial basis, their spatiotemporal dynamics are different. NE at a location would encode often only one decision variable, whereas ACh at one site tends to multiplex and be driven by different behavioral events. To determine behavioral relevance, we activate cholinergic or noradrenergic fibers in the secondary motor cortex using optogenetics to show that increased NE availability selectively promotes exploration during decision-making.

RESULTS

Head-fixed mice play matching pennies against a computer opponent

Matching pennies is a competitive game that involves social and strategic decision-making (*64*, *65*). We previously developed a behavioral paradigm for head-fixed, fluid-restricted mice to play matching pennies against a computer opponent and characterized the behavioral performance in detail (*59*). Briefly, in this iterated version of matching pennies, for each trial, the animal and the computer chose simultaneously the left or right option (Fig. 1A). Outcome was determined by a payoff matrix: If the mouse chose the same option as the computer, the mouse received a water reward; otherwise, there was no reward (Fig. 1B). The computer opponent was programmed to predict the animal's upcoming choice using the choice and outcome history over the session (see Materials and Methods). On the basis of

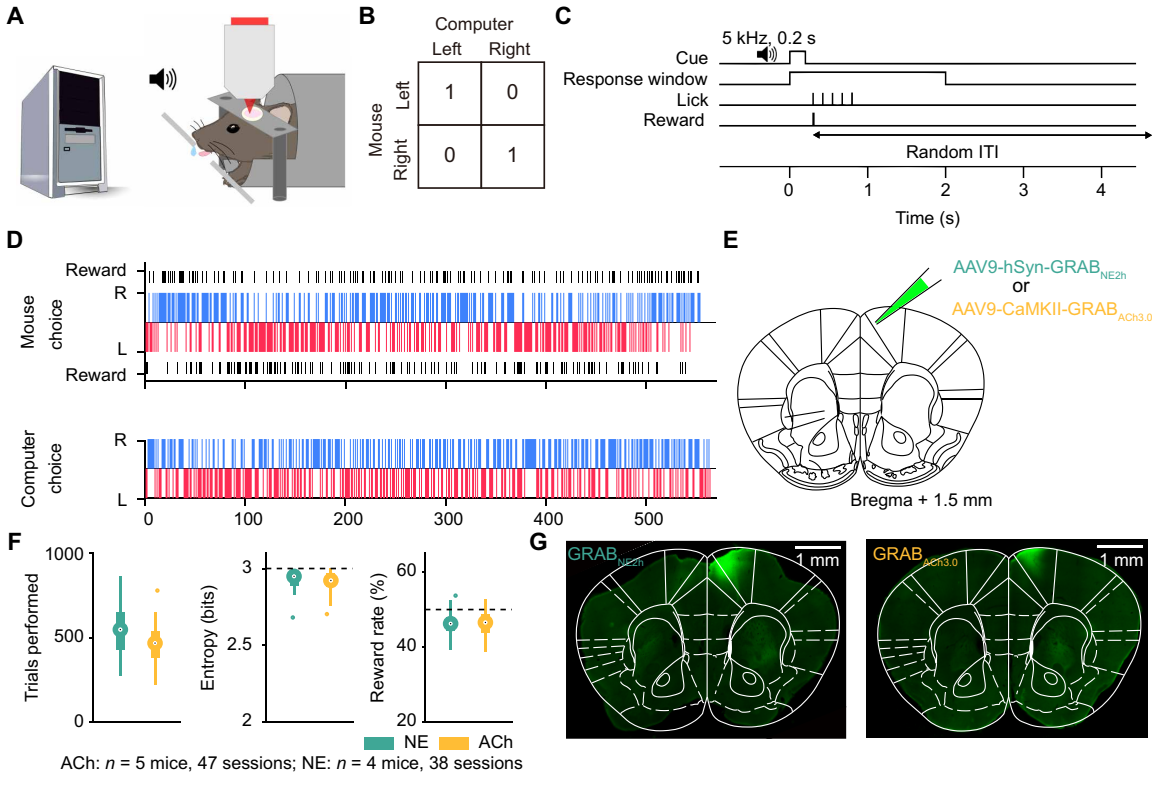

Fig. 1. Head-fixed mice play matching pennies against a computer opponent. (**A**) Schematic of the competitive game. Head-fixed mouse licks left or right spout to indicate left or right choices. A computer tracks the animal's previous choices and outcomes and chooses the side that the mouse is less likely to pick. (**B**) Payoff matrix of the game. The mouse receives a water reward only if it and the computer choose the same action in a trial. (**C**) Each trial, a sound cue signals the start of a response window. The first lick emitted by the animal within the window is logged as the response for that trial, and the outcome is delivered immediately based on the payoff matrix. A random ITI follows the outcome. (**D**) Example session in which the mouse performed at a 50.3% reward rate. Top: The mouse's choices and outcomes. Bottom: The computer's choices. Blue and red bars indicate right and left choices, respectively. Black bars indicate rewards. (**E**) Schematic of the injection site. (**F**) Summary from 38 GRAB$_{NE2h}$ (green) and 47 GRAB$_{ACh3.0}$ (yellow) sessions. Left: The average number of trials performed each session. Middle: The average entropy of three-choice sequences. Right: The average reward rate. (**G**) Post hoc wide-field fluorescence image of GRAB$_{NE2h}$- and GRAB$_{ACh3.0}$-expressing neurons, immunostained with an anti-GFP antibody, in the medial M2 region of the frontal cortex.

the prediction, the computer aimed to provide competitive pressure by selecting the option that the mouse is less likely to pick. At the beginning of each trial, a 0.2-s, 5-kHz sound cue was played to initiate a 2-s response window, during which the mouse could indicate its choice by licking either the left or right spout with its tongue (Fig. 1C). On the basis of the choices of the animal and the computer, a water reward might be delivered at the chosen spout according to the payoff matrix. A random intertrial interval (ITI) was presented to suppress precue licks, which would be prolonged if the animal emitted one or more licks during the interval (see Materials and Methods).

In preparation for characterizing noradrenergic and cholinergic transients, adult C57BL/6J mice were injected with AAV9-hSyn-$GRAB_{NE2h}$ or AAV9-CaMKII-$GRAB_{ACh3.0}$ to express genetically encoded fluorescent indicators of NE (*57*, *58*) and ACh (*56*) in the medial secondary motor cortex (M2), which is the dorsal most aspect of the mouse medial frontal cortex (Fig. 1E). Although the secondary motor cortex includes lateral portion as well, for simplicity, here we will use M2 to specifically refer to this medial portion in the remaining text. We focused on M2 because of its role in action selection during flexible decision-making (*66*–*71*). Headplate and cranial glass window were implanted to enable head fixation and cellular-resolution optical imaging. Animals were trained to reach a stable performance of >40% reward rate for three consecutive sessions. The Nash equilibrium of matching pennies suggests that the optimal play is a mixed strategy: Players should choose left and right with equal probabilities, which would yield a 50% reward rate in the long run. After extensive training, the expert animals made choices with a high degree of stochasticity in a session (Fig. 1D). This contrasts with early sessions when naïve animals were more preservative, choosing with lower entropy, fewer switches, and higher number of miss trials, and consequently exploited by the computer opponent to yield a lower reward rate (fig. S1). The performance metrics stabilized in later sessions as the mice became proficient (fig. S1), indicating that expert animals used a more consistent strategy to play the game.

In total, the dataset involving two-photon imaging during matching pennies included 47 sessions from five expert animals expressing $GRAB_{ACh3.0}$ and 38 sessions from four expert animals expressing $GRAB_{NE2h}$. On average, animals expressing $GRAB_{NE2h}$ and $GRAB_{ACh3.0}$ sensors performed 550 ± 25 and 459 ± 17 trials per session, respectively (means ± SEM, $P = 0.7 \times 10^{-3}$, Wilcoxon rank sum test, FDR_BH adjusted; Fig. 1F). Both groups exhibited a high level of stochasticity in choice behavior, exemplified by the mean entropy values of 2.93 ± 0.01 and 2.91 ± 0.01 for the NE and ACh groups ($P = 0.3$, Wilcoxon rank sum test, FDR_BH adjusted). Accordingly, the animals received reward rates of 46.2 ± 0.5 and 46.2 ± 0.5% ($P = 1.0$, Wilcoxon rank sum test, FDR_BH adjusted), which were near but lower than the optimal reward rate of 50% ($P = 8.0 \times 10^{-7}$ for NE, $n = 4$ mice, 38 sessions; $P = 9.0 \times 10^{-6}$ for ACh, $n = 5$ mice, 47 sessions; Wilcoxon rank sum test, FDR_BH adjusted). Post hoc histology showed the spatial extent of the $GRAB_{NE2h}$ and $GRAB_{ACh3.0}$ expression in the medial frontal cortex, encompassing medial portion of M2 and a small part of Cg1 (Fig. 1G). Together, these results showed that animals undergoing two-photon imaging can play matching pennies at an expert level.

Visualizing frontal cortical NE and ACh transients using genetically encoded fluorescent indicators

We used a two-photon microscope to record fluorescence signals from $GRAB_{NE2h}$ and $GRAB_{ACh3.0}$ sensors at a depth of 100 to 150 μm below the dura (Fig. 2A). The fluorescence signals were diffuse across the field of view (FOV) (Fig. 2, B and C), presumably because the sensors express densely in cell bodies and neuropils. There were typically several dark areas in an FOV, which were likely blood vessels and capillaries. Because of the diffuse signal, we divided the FOV in an unbiased manner by using an evenly spaced grid of 28 × 28 regions of interest (ROIs). Each ROI had an area of 4.46 μm by 4.46 μm. We tested several coarser and finer grid spacings and found that it did not affect the conclusions of the subsequent analyses.

We performed three experiments to confirm that the fluorescence signals arising from $GRAB_{NE2h}$ and $GRAB_{ACh3.0}$ sensors reflect NE and ACh transients in the medial frontal cortex. One, we recorded auditory evoked response because previous studies showed that both noradrenergic neurons in LC and cholinergic neurons in basal forebrain respond to auditory stimuli, particularly unfamiliar and unexpected cues (*42*, *72*). Presentation of 4-kHz, 50-ms auditory cues led to a sharp-rising fluorescent transient from animals that expressed $GRAB_{NE2h}$ or $GRAB_{ACh3.0}$ sensor with similar temporal dynamics (median time-to-peak, $P = 0.7$, Wilcoxon rank sum test; median decay time, $P = 0.2$, Wilcoxon rank sum test; NE: $n = 7$ mice, seven sessions; ACh: $n = 5$ mice, nine sessions; Fig. 2, D to F). Two, cortical cholinergic and noradrenergic axonal activities are correlated with pupillary fluctuations (*21*). We measured spontaneous fluctuations in pupil diameter while imaging $GRAB_{NE2h}$ and $GRAB_{ACh3.0}$ signals in M2 (Fig. 2G). As expected, periods of pupil dilation corresponded roughly to periods of elevated fluorescence signals (Fig. 2H). Collating data from all ROIs across all FOVs, pupil size and fluorescence signals were positively correlated in most ROIs for both $GRAB_{NE2h}$ and $GRAB_{ACh3.0}$ (Fig. 2I). Three, we recorded fluorescence signals from the frontal cortex using $GRAB_{NE2h}$ after administering desipramine. Desipramine is an NE reuptake inhibitor (*73*), and thus we predicted larger fluorescence signals. The $GRAB_{NE2h}$ signal was significantly higher with desipramine than saline control (two-sample *t* tests with Bonferroni correction; saline: $n = 3$ mice, 59 ROIs; desipramine: $n = 3$ mice, 51 ROIs; Fig. 2J), which were normalized to their first imaging frame to account for photobleaching. The application of desipramine also lowered the power of temporal fluctuations at low frequencies and reduced the spatial coherence of $GRAB_{NE2h}$ across ROIs (two-sample *t* tests with Bonferroni correction; saline: $n = 3$ mice, 59 ROIs; desipramine: $n = 3$ mice, 51 ROIs; Fig. 2, K and L). These results provided evidence that the fluorescence signals from $GRAB_{NE2h}$ and $GRAB_{ACh3.0}$ sensors acquired with two-photon microscopy reported fluctuations of NE and ACh levels in the medial frontal cortex.

Frontal cortical NE and ACh transients contain choice- and outcome-related signals

We imaged fluorescence signals to determine NE and ACh transients in M2 as mice played matching pennies against a computer opponent (Fig. 3A). We observed NE and ACh transients that differed for rewarded versus unrewarded trials and contralateral versus ipsilateral choices (Fig. 3B). The animals were trained extensively to have a stereotypical lick response; therefore, the results are similar whether the fluorescence signal was aligned to cue onset or lick onset (fig. S2). To determine more quantitatively how NE and ACh transients in all ROIs relate to behavioral events, we fitted a multiple linear regression model (see Materials and Methods) for each ROI to determine how its fluorescence signal may be explained by choices, outcomes, and reinforcers (choice-outcome interactions) of past

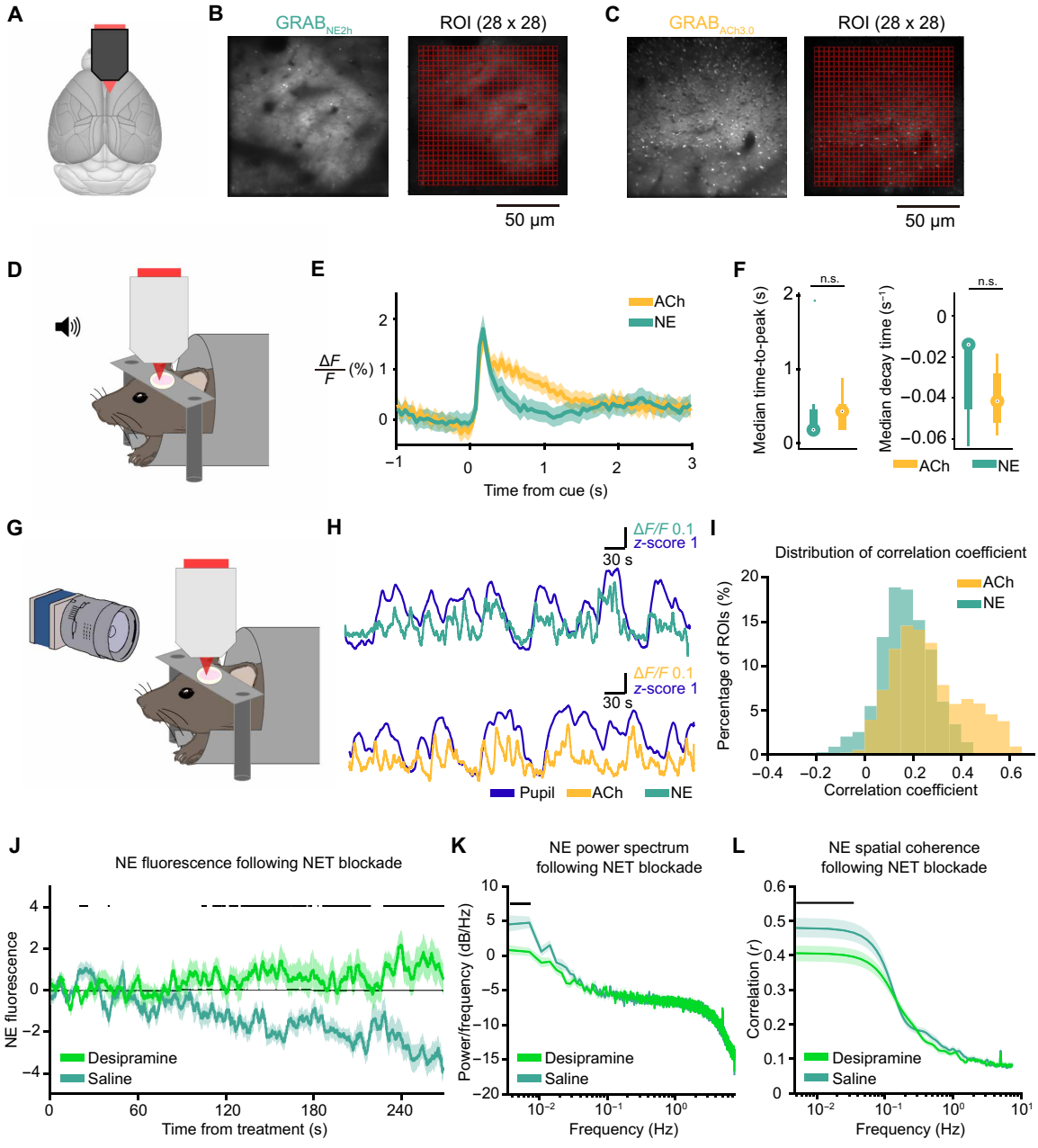

Fig. 2. Visualizing frontal cortical NE and ACh transients using genetically encoded fluorescent indicators. (**A**) Schematic of the imaging site. (**B**) Example FOV of $GRAB_{NE2h}$-expression in layer 2/3 of M2 imaged in vivo with two-photon microscopy. A 28 × 28 grid was used to divide the FOV into ROIs. (**C**) Similar to (B) for $GRAB_{ACh3.0}$. (**D**) Schematic of setup to record auditory evoked response. A 4-kHz, 50-ms auditory stimulus was presented 200 times per session, with simultaneous two-photon imaging. (**E**) Auditory evoked responses averaged across all ROIs and sessions for $GRAB_{NE2h}$ (green) and $GRAB_{ACh3.0}$ (yellow). Shading, 95% confidence interval. (**F**) Temporal parameters of the auditory evoked responses. Left: Median time-to-peak from cue time. $GRAB_{ACh}$: 0.43 (0.18 to 0.53) s; $GRAB_{NE}$: 0.18 (0.18 to 0.45) s. Data are reported as median (25th to 75th percentile). $P = 0.7$, Wilcoxon rank sum test. Right: Median decay time. $GRAB_{NE:}$ −0.01 (−0.04 to −0.01) s^{-1}; $GRAB_{ACh}$: −0.04 (−0.05 to −0.03) s^{-1}. $P = 0.2$, Wilcoxon rank sum test. n.s., not significant. Circle, median. Thick bar, 25th and 75th percentiles. Thin bar, maximum and minimum values. (**G**) Schematic of setup to record pupil diameter. (**H**) Spontaneous pupil diameter in *z*-score (purple) and $GRAB_{NE2h}$ (green) or $GRAB_{ACh3.0}$ (yellow) signal from an example ROI. (**I**) Distributions of maximal coefficients in cross-correlation between pupil dilations and $GRAB_{NE2h}$ (green) or $GRAB_{ACh3.0}$ (yellow) signal. (**J**) $GRAB_{NE2h}$ fluorescence signal averaged across ROIs following treatment with NE reuptake inhibitor desipramine (10 mg/kg, ip, green) or saline (cyan). Shading, 95% confidence intervals. Black dash, time points where $P < 0.05$, two-sample *t* tests with Bonferroni correction. (**K**) Power spectrum for $GRAB_{NE2h}$ signals following desipramine (green) or saline (cyan). Shading, 95% confidence intervals. Black dash, time points where $P < 0.05$, two-sample *t* tests with Bonferroni correction. (**L**) Similar to (K) for spatial coherence.

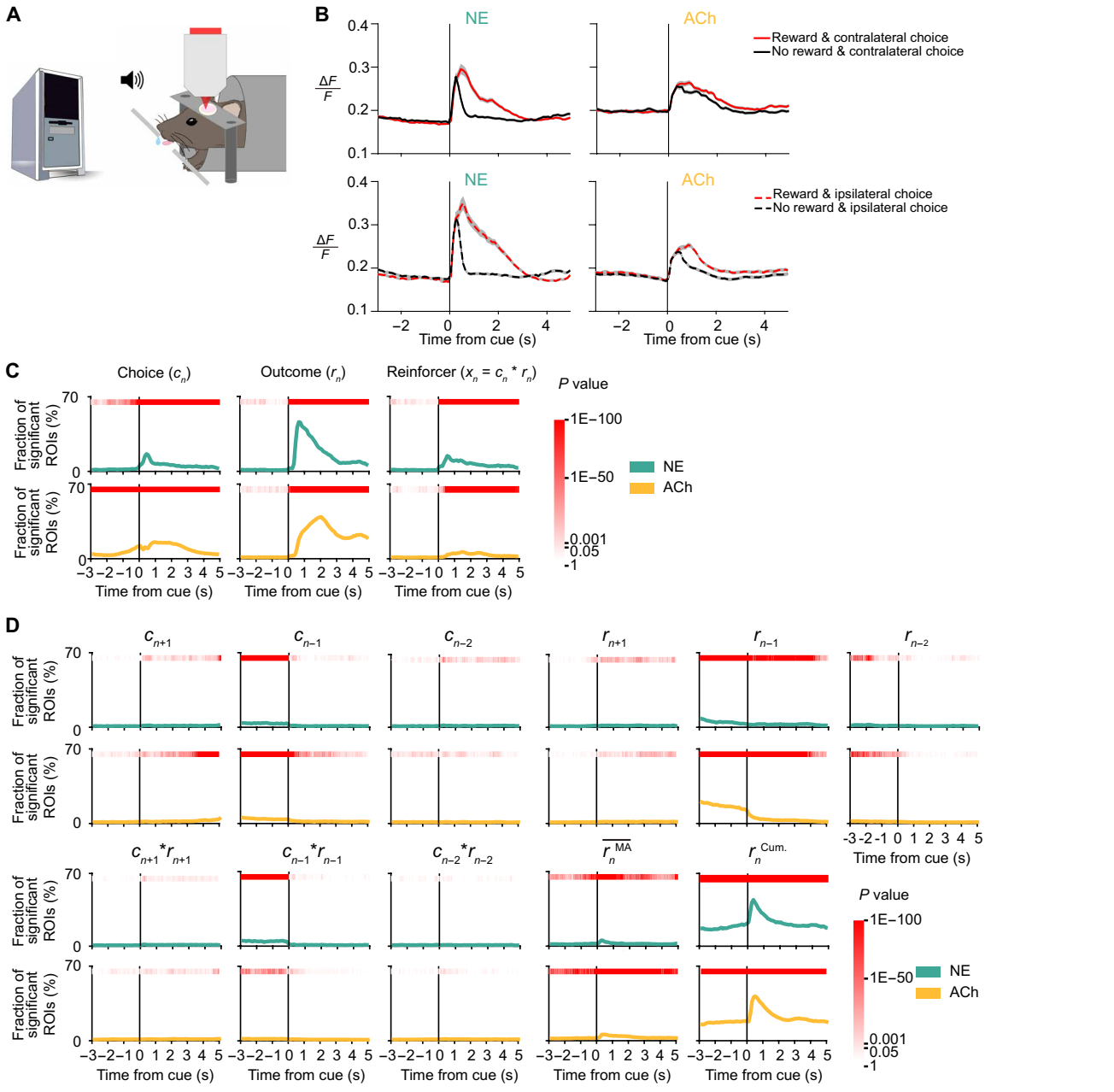

Fig. 3. Frontal cortical NE and ACh transients contain choice- and outcome-related signals. (**A**) Schematic of the mouse playing matching pennies while NE or ACh transients were imaged using two-photon microscopy. (**B**) Trial-averaged fluorescence traces aligned to the cue onset for different subsets of trials. One example ROI was shown each for $GRAB_{NE2h}$ (left) and $GRAB_{ACh3.0}$ (right). Gray shading: 95% confidence interval. (**C**) Proportion of ROIs with significant regression coefficient for choice in the current trial c_n, outcome in the current trial r_n, and reinforcer (choice-outcome interaction) in the current trial x_n in $GRAB_{NE2h}$ (green) and $GRAB_{ACh3.0}$ (yellow) data, determined by fitting a multiple linear regression model. Red shading indicates the *P* value from the chi-square test. (**D**) Fraction of ROIs with significant regression coefficient for choice in the next trial c_{n+1}, choice in the previous trial c_{n-1}, choice in the trial before the previous trial c_{n-2}, outcome in the next trial r_{n+1}, outcome in the previous trial r_{n-1}, outcome in the trial before the previous trial r_{n-2}, reinforcer in the next trial x_{n+1}, reinforcer in the previous trial x_{n-1}, reinforcer in the trial before the previous trial x_{n-2}, recent reward rate r_n^{MA}, calculated as a moving average over last 20 trials, and the cumulative reward r_n^{cum} from start of session to current trial for $GRAB_{NE2h}$ (green) and $GRAB_{ACh3.0}$ (yellow) data determined from the same fit as (B). Red shading indicates the *P* value from the chi-square test.

two, current, and next trials as well as recent reward rate and cumulative reward sum in a session. The results revealed that NE and ACh transients in a sizable fraction of ROIs were modulated by choice, outcome, and reinforcer of the current trial (Fig. 3C; chi-square test; NE: $n = 29{,}792$ observations; ACh: $n = 36{,}848$ observations; against the hypothesized probability of $P = 0.01$). We noted several differences between NE and ACh. For choice, the ACh signal rose before the cue, whereas it was detected in NE only after the cue onset. This is consistent with our earlier finding that pupil-related arousal contained choice information prior to cue (*59*) and indicates that cortical ACh, but not NE, may be involved in the preparation of the upcoming action. There were also differences in the temporal

profiles of the outcome-related ACh and NE signals, which will be examined quantitatively in the next sections. To a lesser degree, ACh and NE levels in M2 were modulated by other behavioral predictors including previous choice, previous outcome, recent reward rate, and cumulative reward sum (Fig. 3D). This analysis showed that NE and ACh transients in M2 vary with decisions during the competitive game. We tested whether switching (choose a different action from the one chosen last trial) was encoded by ACh and NE signals. A linear regression model revealed the representation for switching resembled that of choice (fig. S3), suggesting that encoding of switching, which correlated highly with choices, is an alternative interpretation of the neural data.

To further examine the role of frontal cortical ACh and NE in reinforcement learning, we fitted the animal behavior to a reinforcement learning model with choice kernel (*59*) and then computed how fluorescence signals may be related to latent variables in the model. The results showed some encoding in both NE and ACh activity for latent variables associated with action selection (fig. S4). However, the number of ROIs with significant modulation was small, and there was no clear difference between the ACh and NE groups. Consequently, we did not pursue further analysis relating to the latent variables.

In addition, we noted that the choice and outcome signal might be related to licking behavior as animals lick differently in reward and no reward trials (fig. S5A). To assess how licking might influence the estimation of choice and outcome signals, we constructed a multiple linear regression model that included lick rate as an additional predictor (see Materials and Methods). The results showed a relatively small fraction of ROIs encoding licking, compared to choice and outcome signals (fig. S5, B and C). The inclusion of the lick predictor did not significantly change the fraction of choice- and outcome-related ROIs [NE group, choice-related ROIs, effect of lick: $F(1,5846) = 0$, $P = 0.95$; outcome-related ROIs, effect of lick: $F(1,5846) = 0$, $P = 0.96$; $n = 4$ mice, 38 sessions; ACh group, choice-related ROIs, effect of lick: $F(1,7268) = 0.34$, $P = 0.56$; outcome-related ROIs, effect of lick: $F(1,7268) = 0.02$, $P = 0.88$; $n = 5$ mice, 47 sessions; mixed-effect analysis of variance (ANOVA)]. Although other aspects such as lick onset and lick offset could be additional pertinent factors, this first-pass analysis suggests that the licking behavior was unlikely to affect subsequent analysis.

Spatial organization of the decision-related NE and ACh transients

A key advantage of two-photon imaging is to obtain micrometer-scale maps of the ACh and NE signals (Fig. 4A). Averaging coefficients obtained from multiple linear regression across time suggested that fluorescent transients at different subcellular locations in M2 were linked to behavioral variables differently (Fig. 4B). Figure 4C shows such analysis applied to one FOV, revealing heterogeneity in the spatial distribution of the task representations in the ACh and NE fluctuations. Across all sessions, we found that 81.9 and 83.3% of the ROIs had $GRAB_{NE2h}$ and $GRAB_{ACh3.0}$ transients that were modulated by at least one of the behavioral variables in the multiple linear regression model (Fig. 4D; see Materials and Methods). Focusing on the choice, outcome, and reinforcer in the current trial that constitute the most predictive behavioral variables, 19.2 and 26.9% of the NE and ACh ROIs were significantly modulated by choice (Fig. 4E). Meanwhile, more locations encoded outcomes, encompassing 46.6 and 60.6% of the ACh and NE ROIs. Last, a minority of 18.0 and 9.9% of the NE and ACh ROIs were associated with reinforcer. A single ROI may be significantly modulated by more than one behavioral variable. This might happen because (i) locations represent behavioral variables with independent probabilities and overlap by chance or (ii) locations may preferentially have correlated representation of multiple behavioral variables. The second explanation was supported by statistical tests because the overlap of ROIs modulated by different behavioral variables occurred at a rate higher than chance for both ACh and NE ($P = 0$, $P = 0$, $P = 0$, for overlap between choice- and outcome-, choice- and reinforcer-, and outcome- and reinforcer-modulated ROIs, respectively; Pearson independent test; NE, $n = 29{,}792$ total observations; ACh, $n = 36{,}848$ total observations). The data were organized into a 2×2 contingency table (table S1).

To gain insight into the spatial integration of behaviorally relevant ACh and NE signals, we calculated the conditional probabilities that an ROI encoded one variable v_1 given that it also encoded another variable v_2 [$Pr(v_1|v_2)$]. A head-to-head comparison of these conditional probabilities between NE and ACh highlighted a significantly higher degree of multiplexed coding of task information by ACh transients, as evident from the higher $Pr(r_n|c_n)$, $Pr(r_n|x_n)$, and $Pr(c_n|x_n)$ values ($P = 0.044$, $P = 0.034$, and $P = 0.030$; median test; NE: $n = 4$ mice, 38 sessions; ACh: $n = 5$ mice, 47 sessions; Fig. 4, F and G, and table S2). We did not detect a difference in $Pr(c_n|r_n)$ ($P = 0.864$; median test. NE: $n = 4$ mice, 38 sessions; ACh: $n = 5$ mice, 47 sessions; Fig. 4G). The $Pr(x_n|c_n)$ and $Pr(x_n|r_n)$ values were shown for completeness ($P = 0.002$ and $P = 0.072$; median test; NE: $n = 4$ mice, 38 sessions; ACh: $n = 5$ mice, 47 sessions; Fig. 4H), but they represented a small number of ROIs due to fewer locations encoding reinforcer. Together, frontal cortical ACh transients are more likely to multiplex task-related information, where NE transients encode behavioral events in a more spatially segregated manner.

Distinct temporal dynamics of the task-related NE and ACh signals

The most prominent behavioral readout linked to frontal cortical NE and ACh transients was outcome; therefore, we asked how the reward-related signals evolve over time at different locations. To understand the spatiotemporal dynamics, we used the regression coefficient for outcome extracted for each ROI that was significantly modulated by outcome, based on the result in Fig. 4E (fig. S6, A and C). These traces were sorted using hierarchical clustering based on Pearson correlation (Fig. 5A). The correlation matrices of the sorted regression coefficients revealed two clusters of ROIs for NE and ACh (Fig. 5B). For group 1, which captured 92.4 and 93.4% of the ROIs for NE and ACh, respectively, the occurrence of a reward increased fluorescence signal (Fig. 5C). The temporal dynamics of NE and ACh signals differ because NE signals rose faster and were more temporally aligned than ACh as reflected by the shorter median time-to-peak and smaller variance of time-to-peak ($P = 1.54 \times 10^{-13}$ and $P = 0.002$, respectively; Wilcoxon rank sum test; NE: $n = 4$ mice, 38 sessions; ACh: $n = 5$ mice, 47 sessions ROIs; Fig. 5D, left and middle, and table S3). The peak value of the regression coefficient was larger in NE than ACh ($P = 0.003$; Wilcoxon rank sum test; NE: $n = 4$ mice, 38 sessions; ACh: $n = 5$ mice, 47 sessions; Fig. 5F, right, and table S3), although this magnitude depended on experimental factors such as fluorophore expression level (*74*) and therefore should be interpreted with caution. For group 2, which only captured 7.6 and 6.6% of the ROIs for NE and ACh, respectively, the

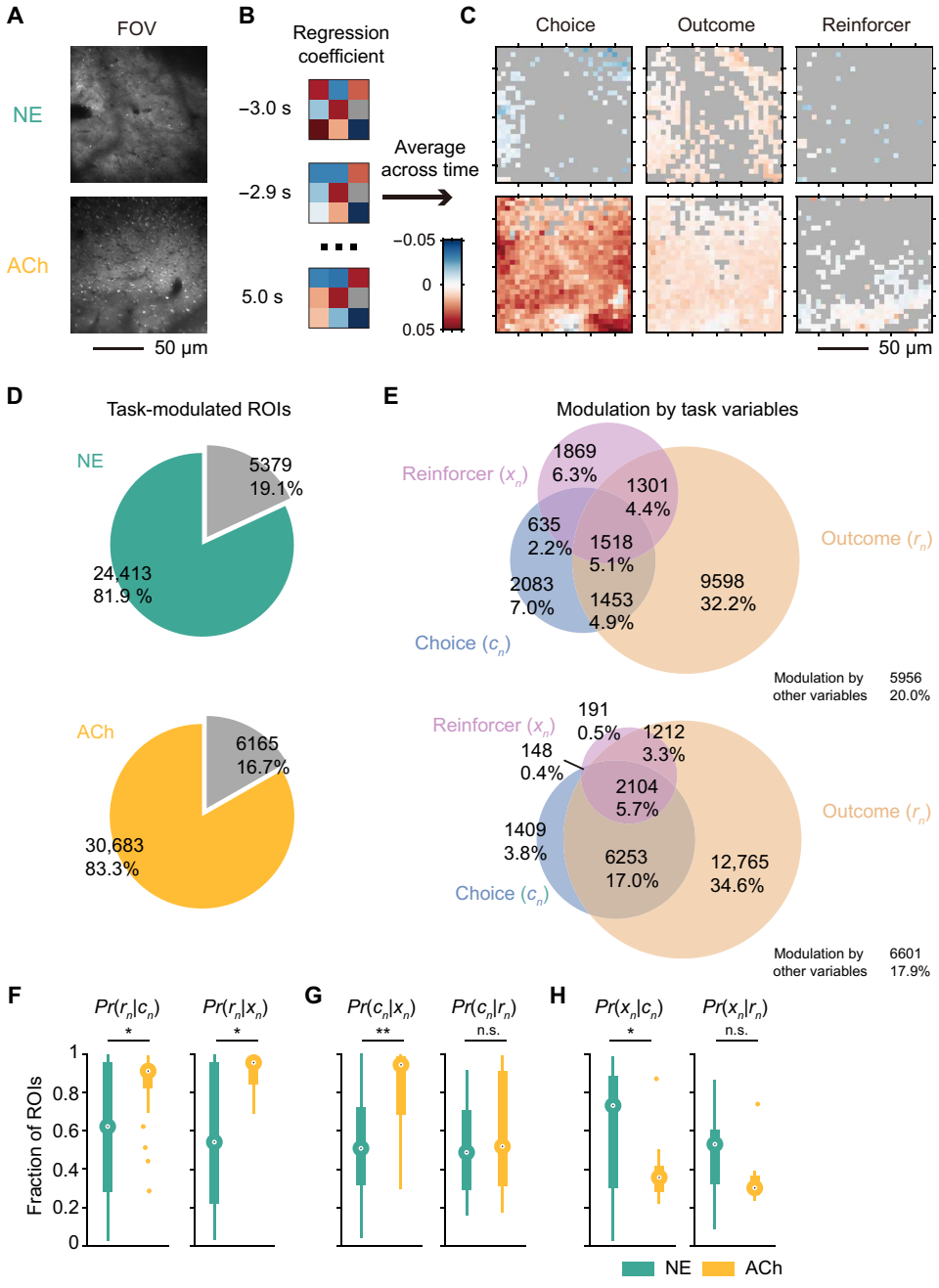

Fig. 4. Spatial organization of the decision-related NE and ACh transients. (**A**) Example FOVs (same as Fig. 2, B and C) of $GRAB_{NE2h}$ (top) and $GRAB_{ACh3.0}$ (bottom) expression in layer 2/3 of M2. (**B**) Schematic illustrating the analysis: For each ROI in an FOV, the regression coefficients over $t = -3$ to 5 s was averaged and plotted in pseudocolor. (**C**) Spatial maps of mean regression coefficients for choice (left), outcome (middle), and reinforcer (right) for the $GRAB_{NE2h}$ (top row) and $GRAB_{ACh3.0}$ (bottom row) FOVs shown in (A). (**D**) Venn diagrams showing the number and percentage of ROIs that were significantly modulated by at least one task-related variable. (**E**) Venn diagrams showing the number and percentage of ROIs that were significantly modulated by the current choice, outcome, and reinforcer. (**F**) Boxplot of the conditional probabilities in $GRAB_{NE2h}$ (green) and $GRAB_{ACh3.0}$ (yellow) data. Median test, $Pr(r_n|c_n)$: $P = 0.044$; $Pr(r_n|x_n)$: $P = 0.034$. $^*P < 0.05$; $^{**}P < 0.01$; n.s., not significant. Large circles, medians. Thick bars denote 25th and 75th percentiles. Lines end at maximum and minimum value. Small circles, outliers. (**G**) Same as (F) for $Pr(c_n|x_n)$: $P = 0.002$; and $Pr(c_n|r_n)$: $P = 0.864$. (**H**) Same as (F) for $Pr(x_n|c_n)$: $P = 0.002$; and $Pr(x_n|r_n)$: $P = 0.072$.

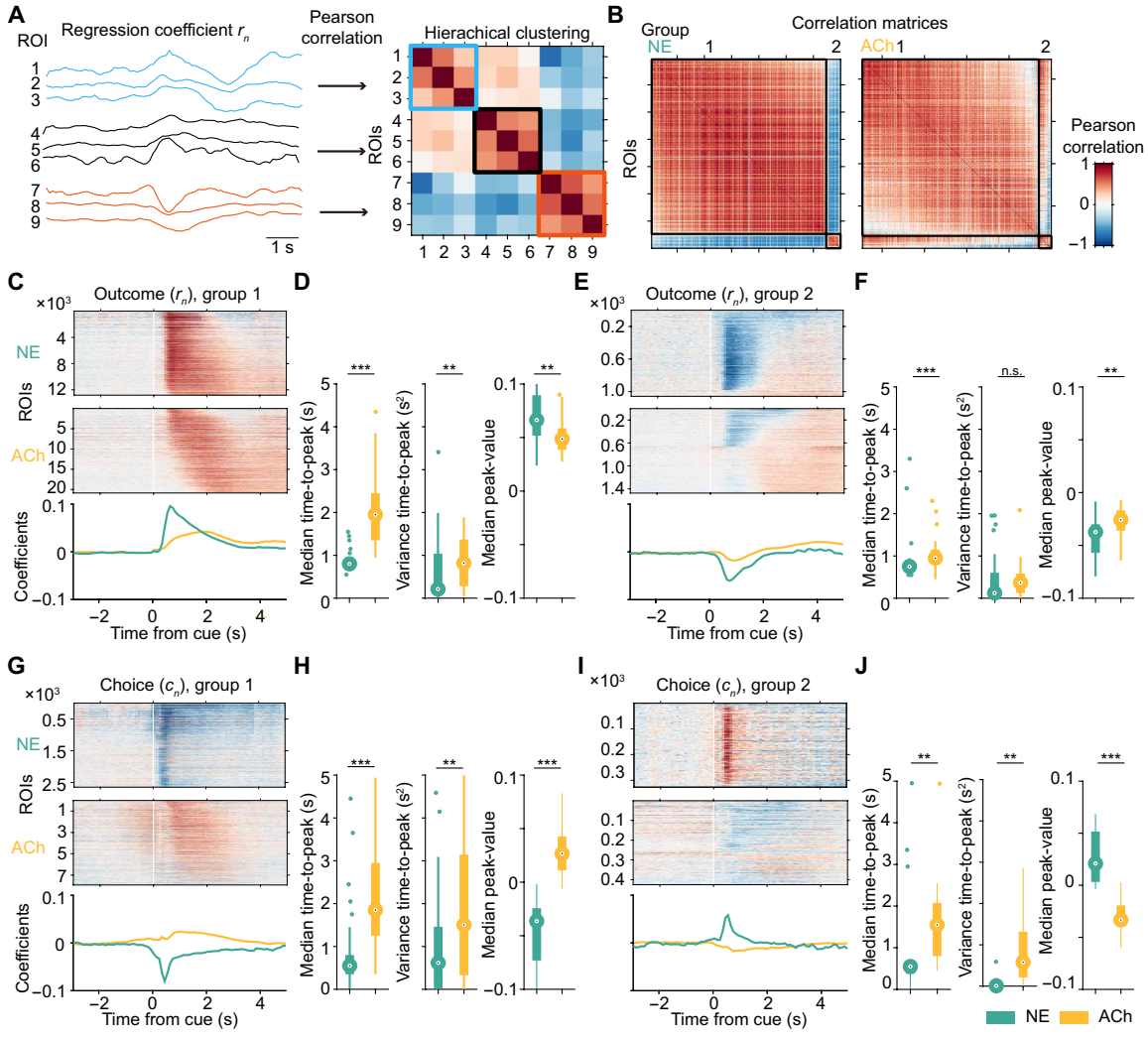

Fig. 5. Distinct temporal dynamics of the task-related NE and ACh signals. (**A**) Schematic illustrating the analysis: Regression coefficients for current outcome were clustered into different groups using hierarchical clustering based on Pearson correlation. (**B**) Correlation matrices showing the clustering results for $GRAB_{NE2h}$ (left) and $GRAB_{ACh3.0}$ (right). (**C**) Top: Heatmap of regression coefficients for current outcome for ROIs in group 1. Bottom: Average regression coefficient for current outcome for ROIs in group 1 for $GRAB_{NE2h}$ (green) and $GRAB_{ACh3.0}$ (yellow). (**D**) Temporal parameters of outcome-related activity in group 1 for $GRAB_{NE2h}$ (green) and $GRAB_{ACh3.0}$ (yellow) data. Wilcoxon rank sum test. Left: Median time-to-peak, $P = 1.54 \times 10^{-13}$. Middle: Variance time-to-peak, $P = 0.002$. Right: Median peak-value, $P = 0.003$. $^{**}P < 0.01$; $^{***}P < 0.001$; n.s., not significant. Large circle, median. Thick bar, 25th and 75th percentiles. Thin line, maximum and minimum values. Small circle, outlier. (**E** and **F**) Similar to [(C) and (D)] for ROIs in group 2. Median time-to-peak, $P = 1.43 \times 10^{-4}$. Variance time-to-peak, $P = 0.108$. Median peak-value, $P = 0.002$. (**G** and **H**) Similar to [(C) and (D)] for regression coefficient for current choice for ROIs in group 1. Median time-to-peak, $P = 1.06 \times 10^{-7}$. Variance time-to-peak, $P = 0.003$. Median peak-value, $P = 3.53 \times 10^{-14}$. (**I** and **J**) Similar to [(C) and (D)] for regression coefficient for current choice for ROIs in group 2. Median time-to-peak, $P = 0.022$. Variance time-to-peak, $P = 0.001$. Median peak-value, $P = 1.88 \times 10^{-7}$.

occurrence of a reward reduced fluorescence signal (Fig. 3E). There were similar differences in temporal dynamics for ROIs in group 2 as for those in group 1, except the difference in variance of time-to-peak was not statistically significant (median time-to-peak, $P = 1.43 \times 10^{-4}$; variance time-to-peak, $P = 0.108$; median peak-value, $P = 0.002$; Wilcoxon rank sum test; NE: $n = 4$ mice, 38 sessions; ACh: $n = 5$ mice, 47 sessions; Fig. 5F and table S3).

We clustered the ROIs based on their regression coefficient for outcome, but what about the choice-related signals, given that there is spatially correlated encoding of behavioral variables? We plotted the subset of ROIs with significant choice encoding, on the condition that these ROIs were significantly modulated by outcome, using the same grouping and sorted ranking (Fig. 5, G and I, and fig. S6, B and D). The timing of the choice-related ACh and NE signals was also different: the choice-related NE signals emerged earlier and were more synchronized than ACh (group 1: median time-to-peak, $P = 1.06 \times 10^{-7}$; variance time-to-peak, $P = 0.003$; median peak-value, $P = 3.53 \times 10^{-14}$; group 2: median time-to-peak, $P = 0.022$; variance time-to-peak, $P = 0.001$; median peak-value, $P = 1.88 \times 10^{-7}$; NE: $n = 4$ mice, 38 sessions; ACh: $n = 5$ mice, 47 sessions; Wilcoxon rank sum test; Fig. 5, H and J, and table S3). Notably, the sign of the regression coefficients for choice was opposite for NE and ACh. Although choice led to elevations of both NE and ACh in M2, NE was preferentially driven by ipsilateral choice whereas ACh

was more responsive to contralateral choice (Fig. 5H). To provide a more complete picture, we also show the ACh and NE signals in ROIs that were choice- and outcome-related (fig. S6, E and G) or only choice-related (fig. S6, F and H). These results reveal that decision-related NE signals were more synchronized and peaked earlier than ACh transients in M2.

Optogenetic elevation of frontal cortical NE increases switch probability

Given that NE and ACh transients exhibit task-related signals with distinct spatial and temporal dynamics, we wanted to know whether their levels in M2 may differentially contribute to behavioral performance. To causally test the roles of the neuromodulators, we used optogenetics to stimulate noradrenergic and cholinergic axons in M2 as mice engaged in the matching pennies game (Fig. 6, A and B). The payoff matrix and trial structure were the same as the one used in imaging experiments except for the additional laser photostimulation on select trials (Fig. 6C). Photostimulation (473 nm, 40 Hz) would start at cue onset and sustain until 1 s, targeting one location in one of the hemispheres, after the mouse makes a choice (i.e., the first lick within the response window). This was designed to roughly mimic the time course of the observed NE and ACh transients in M2. We used a laser steering system that can rapidly reposition the laser beam, and mice were implanted with a clear skull cap (see Materials and Methods), which allowed us to photostimulate a different region in the dorsal cortex on each trial. To target noradrenergic neurons, we crossed a knock-in Dbh-Cre mouse (*75*) with the Ai32 strain (*76*) for Cre-dependent expression of ChR2. To target noradrenergic neurons, we crossed a ChAT-Cre mouse (*77*) with the Ai32 strain for Cre-dependent expression of ChR2. Post hoc immunostaining and confocal microscopy of fixed coronal sections confirmed ChR2 expression in axons in M2 (Fig. 6D).

Initially, we tested how optogenetic stimulation of noradrenergic and cholinergic axons in different brain regions may contribute to performance in matching pennies. We stimulated four regions including the left and right secondary motor cortex and left and right primary visual cortex (left M2, right M2, left V1, and right V1; 40% chance of photostimulation on a given trial, equally allocated to each region) in a single session while fixing the power at one of three levels for the session (0, 1.5, and 3 mW; Fig. 6E). The visual cortical regions were chosen as a potential control because we expect its function to not be required during matching pennies, which does not involve a visual stimulus. The most obvious effect of photostimulation was to alter the probability of a choice switch on the subsequent trial (i.e., if the mouse chose left and received a photostimulation, then the next trial it would choose right, and vice versa). With increasing power, we observed that evoking NE release in M2 increased the tendency for the mouse to change its choice [main effect of power: $F(75,2) = 7.57$, $P = 0.001$, two-way ANOVA and Tukey post hoc test, $n = 6$ mice, 76 sessions] (Fig. 6F and table S4). Curiously, this consequence of NE manipulation was equally effective for all regions stimulated [main effect of region: $F(75,4) = 0.11$, $P = 0.98$; interaction of region and power: $F(75,8) = 0.05$, $P = 1.00$]. Similarly, there was a significant effect of photostimulation power on the switch probability [$F(90,2) = 8.39$, $P = 0.0005$, $n = 6$ mice, 76 sessions]. We wanted to know whether this photostimulation-induced propensity to alternate choices affected performance. Comparing sessions with increasing laser power, we did not detect any difference on performance metrics including entropy [NE: $F(41,2) = 0.90$, $P = 0.42$; ACh: $F(43,2) = 0.20$, $P = 0.82$; one-way ANOVA], number of trials performed per session [NE: $F(44,2) = 1.64$, $P = 0.21$; ACh: $F(43,2) = 0.48$, $P = 0.62$], or reward rate [NE: $F(44,2) = 1.09$, $P = 0.35$; ACh: $F(43,2) = 0.009$, $P = 0.99$; NE: $n = 6$ mice, 76 sessions; ACh: $n = 7$ mice, 91 sessions] (Fig. 6G and table S5). Collectively, this photostimulation protocol increases the switch probability for both the Dbh-Cre;Ai32 and ChAT-Cre;Ai32 mice. The behavioral alterations lacked region and temporal specificity because the choice behavior was altered on trials when any region was stimulated or even when photostimulation was absent.

We speculated that the lack of region and temporal specificity for the protocol shown in Fig. 6E may be because the photostimulation trials were too frequent. Therefore, we modified the protocol to activate only one region at 3 mW on 10% of the trials per session (Fig. 6H). With this revised photostimulation protocol, we observed a within-session difference for NE between the photostimulation and control trials [main effect of photostimulation: $F(40,1) = 5.62$, $P = 0.02$, two-way ANOVA, $n = 6$ mice, 41 sessions], with the mouse switching its choice significantly more on trials following optogenetic stimulation of noradrenergic axons compared to trials without ($P = 0.022$, Tukey post hoc test; Fig. 6I and table S6). We did not detect region specificity for the NE photostimulation [interaction of photostimulation x region: $F(40,3) = 0.37$, $P = 0.8$, $n = 6$ mice, 41 sessions]. Because no difference was detected between M2 and V1 in the left and right hemispheres, we combined the data of left and right M2, as well as left and left V1 in Dbh-Cre data, which did not change the result (table S7). The lack of region specificity is likely due to the interconnected, branching afferents of NE neurons, and our photostimulation is activating collaterals to project to multiple other cortical regions (*38*, *43*). With this protocol, we did not detect behavioral changes when manipulating ACh levels [main effect of region: $F(48,3) = 0.99$, $P = 0.40$; main effect of stimulation: $F(48,1) = 0.07$, $P = 0.80$, $n = 7$ mice, 49 sessions]. There was no impact of the photostimulation on the whole-session performance metrics (Fig. 6J and table S8). Given the significant behavioral effects for NE, we did two further analyses to understand the phenomenon. The first analysis revealed that the increase in switching probability was most pronounced for the first trial after photostimulation and did not extend to subsequent trials except for M2-R where there was a prolonged effect for two trials (fig. S7 and table S9). The second analysis showed that mice tended to stay following a reward, and this is specifically when NE was effective at promoting switching behavior (fig. S8 and table S10). Together, considering the results from both photostimulation protocols, we concluded that optogenetic stimulation of noradrenergic axons increases the switch probability on the subsequent trial, with regional preference and temporal specificity if the photostimulation was applied sparsely.

Optogenetic elevation of frontal cortical NE in a simple choice task

Because optogenetic activation of noradrenergic axons in M2 promoted switching without improving reward rate, we wondered whether the impact of the perturbation was specific to decision-making with competitive pressure like matching pennies or whether the effect would generalize to a simplified task. We trained the same mice, after matching pennies experiments, on a simple choice task where there is no inherent benefit to switching (Dbh-Cre: $n = 6$ mice, 12 sessions; ChAT-Cre: $n = 4$ mice, 8 sessions). The structure and timing of each trial was nearly identical to matching pennies

(Fig. 7, A and B). Photostimulation (473 nm, 40 Hz, 3 mW) applied to M2 occurred on select trials starting at the choice and sustained for 1 s. Different from matching pennies, instead of a payoff matrix, reward availability followed a block structure (Fig. 7C). In block 1, left choices have a 50% chance of water reward whereas right choices have a 50% chance of water reward paired with photostimulation. After a random number of trials, without external cue informing the mouse of the block reversal, block 2 began with the opposite action-outcome contingencies. Each mouse was tested on multiple sessions with either sham photostimulation (0 mW) or photostimulation at 3 mW in a randomized order. Example sessions illustrated the typical behavior: Without photostimulation, Dbh-Cre;Ai32 and ChAT-Cre;Ai32 mice tended to stick to one option and would persist in making the same choice repeatedly (Fig. 7, D and F). However, a Dbh-Cre;Ai32 mouse switched more frequently when the water reward was paired with photostimulation than control (Fig. 7E). By contrast, a ChAT-Cre;Ai32 mouse switched rarely even when photostimulation was active (Fig. 7G). Summarizing the data across all animals, mice completed a similar number of trials per session regardless of photostimulation [Dbh-Cre;Ai32: $t(11) = 0.28$, $P = 0.79$; ChAT-Cre;Ai32: $t(8) = 0.88$, $P = 0.40$; Fig. 7H, left]. Dbh-Cre;Ai32 mice overall explored the options more by switching choices during a session with photostimulation [$t(11) = -2.68$, $P = 0.02$], whereas ChAT-Cre;Ai32 mice switched infrequently in both conditions [$t(8) = 0.65$, $P = 0.53$; Fig. 7H, right]. Analyzing the data on a per-trial basis, neither strain showed a preference for the side designated for photostimulation [Dbh-Cre;Ai32: $t(11) = -1.45$, $P = 0.18$; ChAT-Cre;Ai32: $t(8) = -1.24$, $P = 0.25$, Fig. 7I, left]. Dbh-Cre;Ai32 mice were more likely to switch on any given trial in sessions with photostimulation [$t(11) = -2.55$, $P = 0.03$], whereas ChAT-Cre;Ai32 mice showed no difference [$t(8) = 0.30$, $P = 0.77$; Fig. 7I, right]. These results indicate that the evoked elevation of NE in M2 causes the mouse to switch choices more frequently, although there is no preference for photostimulation per se and there is no incentive in this simple choice task for exploring.

DISCUSSION

This study yielded three main findings. First, during a competitive game, both NE and ACh in the mouse M2 encode task-relevant information including choice and outcome. The noradrenergic representation is more spatially segregated at the subcellular scale, whereas the cholinergic representation tends to multiplex multiple behavioral variables at the same location. Second, the decision-related NE transients are more synchronized and peak earlier than the ACh signals. Third, elevating NE levels in M2 promotes exploratory behavior by spurring the animal to switch choices on the subsequent trial. Together, these findings reveal distinct spatiotemporal dynamics for NE and ACh signaling in the frontal cortex, which may underpin their differential contributions to learning and decision-making.

Imaging considerations

We can visualize the dynamic fluctuation of neuromodulator levels at subcellular resolution owing to advances in genetically encoded fluorescent sensors of NE and ACh. However, there are limitations to consider. Two-photon-excited fluorescence enables deep-tissue imaging, but the dense expression and relatively weak brightness of the current generation of sensors restrict the imaging depth. Therefore, we are only sampling NE and ACh transients in the supragranular layers of M2. For NE, most LC inputs to the cortex resides in layer I (*78*). However, we are likely missing a substantial fraction of cholinergic inputs because afferents from the basal forebrain predominantly reside in infragranular layers, with 77% found in layers V and VI, and only 14 and 9% in layer I and layer II/III, respectively (*79*). We obtained ~10% change in fractional fluorescence from the most responsive ROIs and ~1 to 2% change in fractional fluorescence averaged across an FOV. We were concerned that fluorescence signals may arise from motion artifact, rather than biological sources. This is why we performed the auditory evoked response and spontaneous pupillary measurements to confirm that the fluorescence signals agree with known physiological correlates of cortical NE and ACh levels.

A main finding of this study is the difference in timing, where task-related elevation of NE was significantly more aligned and peaked shortly after the decision. The τ_{on} and τ_{off} are 0.11 and 0.58 s for $GRAB_{ACh3.0}$ for 100 μM ACh (*56*), whereas the τ_{on} and τ_{off} are 0.09 and 1.93 s for $GRAB_{NE2h}$ for 100 μM NE (*58*). The sensors have similar rise times and $GRAB_{NE2h}$ has slower decay time than $GRAB_{ACh3.0}$; therefore, the intrinsic kinetics of the sensors cannot account for the temporal dynamics observed in this study. We observed that ACh transients have variable rise time (Fig. 5, D and H), such that, in aggregate, the front al cortical ACh elevation is elongated relative to NE. The temporal dynamics of the different neuromodulators are governed not only by release but also by the reuptake transporters in the vicinity, which may be behaviorally relevant. There is effort to expand the color palette of the genetically encoded fluorescent sensors. Red-shifted sensors are available now for dopamine (*80*, *81*) and have just been developed for NE (*82*). Future studies may leverage wavelength-shifted sensors to simultaneously monitor multiple neuromodulators at the same time to further determine whether the spatial organization of ACh and NE transients may be coordinated and the potential interplay between different neuromodulators, which were hinted by studies showing that the level of a neuromodulator, can alter the release of another neuromodulator (*83*, *84*).

Spatial organization of decision-related NE and ACh transients in the medial frontal cortex

Our results reveal that NE and ACh transients of the mouse M2 occur when animals made choices and received rewards during a competitive decision-making task. Fluctuations of cholinergic and noradrenergic activities are intimately linked to pupil-associated arousal state (*21*); therefore, our results are consistent with prior works showing that pupil size changes are correlated with choice, outcome, and reward prediction error (RPE) (*59*, *85*–*87*). Moreover, the finding of this study is in agreement with a recent study reporting that cholinergic basal forebrain neurons provide reinforcement signals to its axonal targets (*88*). Although we chose to focus on medial M2 because of its leading role in action selection (*71*, *89*), future studies may consider studying other brain regions such as the anterior lateral motor cortex (ALM).

A notable conclusion of this study is that the decision-related signals carried by NE are more spatially distributed at the subcellular scale, whereas ACh can be modified by multiple behavioral variables at the same location. Representation of different behavioral variables at the subcellular scale has been observed previously in the dopamine system. Using two-photon microscopy to visualize calcium transients, individual dopaminergic axons in the dorsal striatum were found to

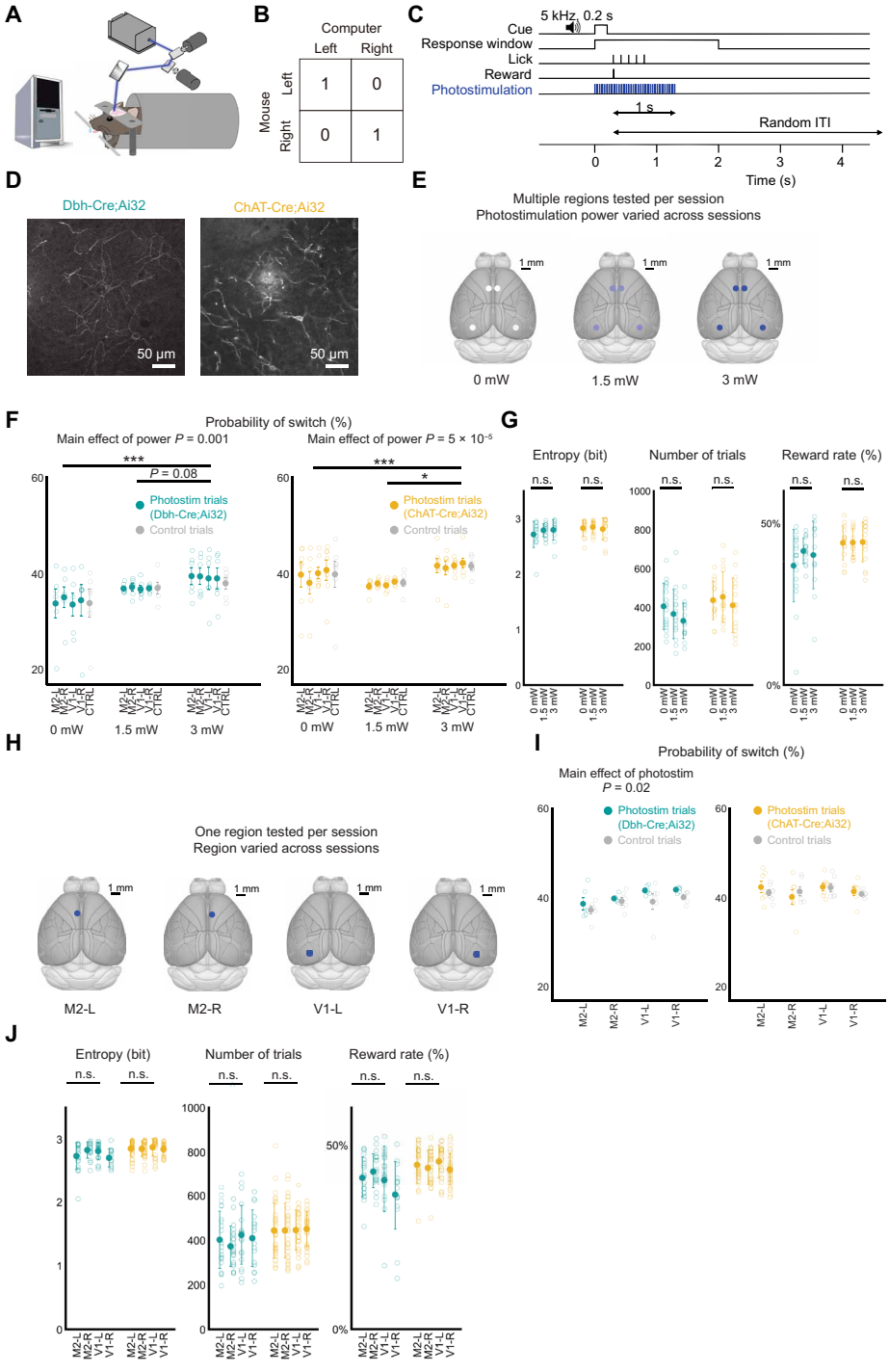

Fig. 6. Optogenetic elevation of frontal cortical NE increases switching in matching pennies. (**A**) Schematic of the mouse playing matching pennies while noradrenergic and cholinergic axons were stimulated via optogenetics using a laser-steering system. (**B**) Payoff matrix of the game. (**C**) Timing of each trial. On trials with photostimulation, laser turns on at cue onset and sustains until 1 s after choice. (**D**) Confocal micrographs of immunostained axons in the coronal section of M2 of Dbh-Cre;Ai32 (left) and ChAT-Cre;Ai32 (right) mice. (**E**) Schematic of the protocol to test effects of region within session and power across sessions. Dbh-Cre: $n = 6$ mice, 76 sessions; ChAT-Cre: $n = 7$ mice, 91 sessions. Multiple regions were tested per session, with maximum of one region tested per trial. A total of 40% of trials are stimulated with 10% allocated to each region (M2-L, M2-R, V1-L, and V1-R). One power level is tested per session. (**F**) Probability of switch on trial after photostimulation by region and power. (**G**) Session-based performance metrics, including entropy (left), number of trials (middle) and reward rate (right). (**H**) Schematic of protocol to test effects of region-specific photostimulation across sessions. One region was tested per session. A total of 10% of trials are stimulated at 3 mW. Dbh-Cre: $n = 6$ mice, 41 sessions; ChAT-Cre: $n = 7$ mice, 49 sessions. (**I**) Probability of switch on trial after photostimulation by region. (**J**) Session-based performance metrics, including entropy (left), number of trials (middle), and reward rate (right). Statistical analyses were performed using two-way ANOVA for (F) and (I) and one-way ANOVA for (G) and (J) and are included in supplementary tables. *$P < 0.05$; ***$P < 0.001$; n.s., not significant.

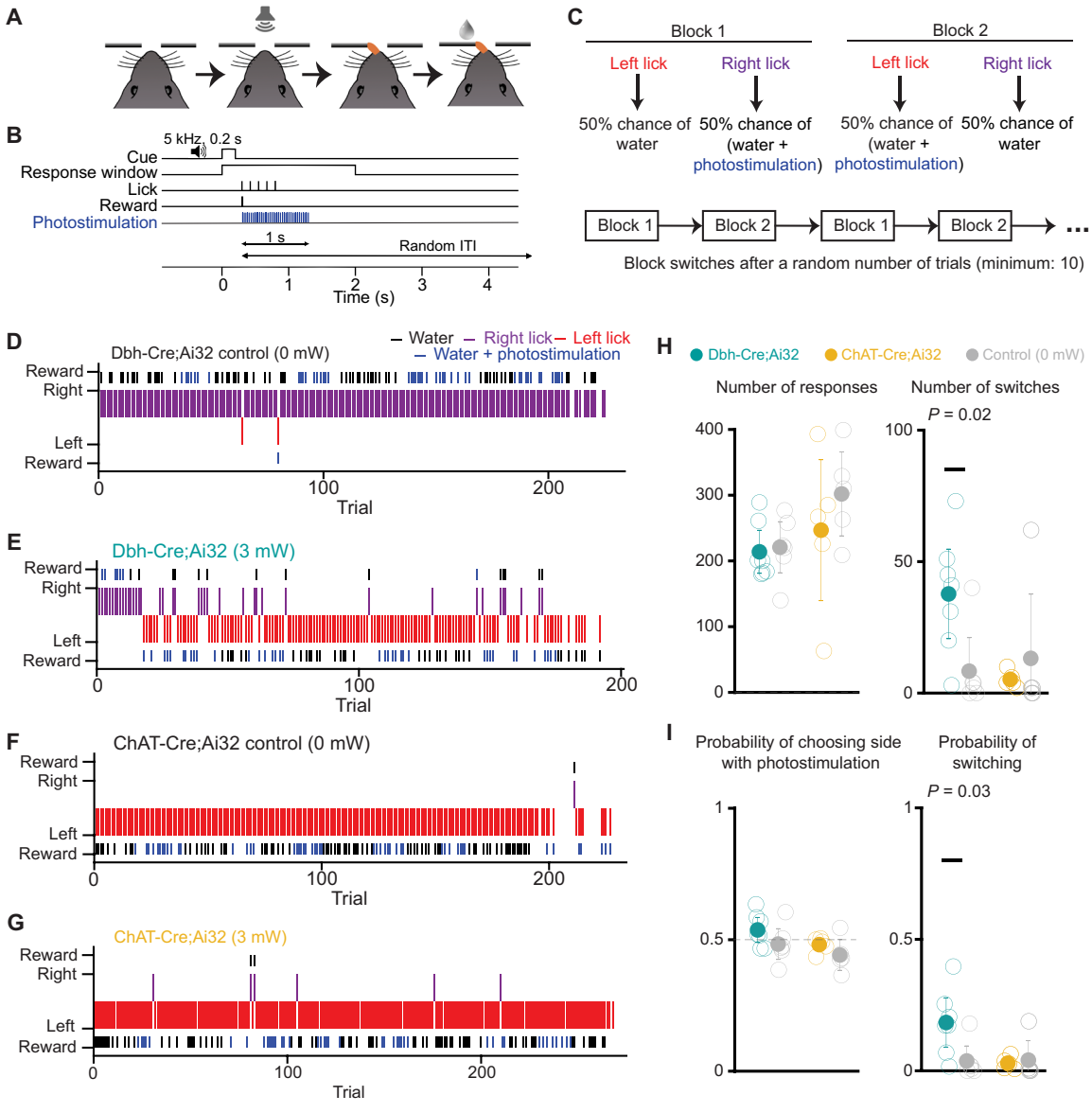

Fig. 7. Optogenetic elevation of frontal cortical NE increases switching in a simple choice task. (**A**) Schematic of simple choice task. (**B**) Each trial, a sound cue signals the start of a response window. The first lick emitted by the animal within the window is logged as the response for that trial, and the outcome is delivered immediately according to the trial block structure. A random ITI follows the outcome. On trials with photostimulation, laser turns on at time of choice and sustains until 1 s after choice. (**C**) Schematic of the trial block structure. For trials in block 1, a left lick leads to water 50% of the time and a right lick leads to water paired with photostimulation 50% of the time. For trials in block 2, action-outcome contingencies are reversed. The first block is randomly selected. The block type reverses after a random number of choices (drawn from a truncated exponential distribution, with a minimum number of 10 trials). (**D**) Example session for a Dbh-Cre;Ai32 mouse with sham stimulation. (**E**) Same mouse as in (D) but in a session with 3-mW photostimulation. (**F**) Example session for a ChAT-Cre;Ai32 mouse with sham stimulation. (**G**) Same mouse as in (F) but in a session with 3-mW stimulation. (**H**) Quantification for session-based metrics including number of responses (left) and switches (right). (**I**) Quantification for trial-based metrics including probability of choosing side designated for photostimulation (left) and probability of switching (right). Dbh-Cre: $n = 6$ mice, 12 sessions; ChAT-Cre: $n = 4$ mice, 8 sessions.

encode either locomotion onset or reward (*90*). The heterogeneity in behavioral correlates mapped onto genetically defined subtypes of dopaminergic neurons (*91*). Recent studies have likewise revealed subtypes of noradrenergic neurons in the LC, with distinct firing patterns during decision-making (*92*) and preferential long-range projection targets (*93*, *94*). There are also subtypes of cholinergic neurons in the basal forebrain, which differ in physiological properties and behavioral correlates (*95*). Because previous rat and mouse studies reported a higher density of cholinergic axons than noradrenergic axons in the cortex (*96*–*98*), it is plausible that the spatial organization of ACh and NE transients arises due to various degrees of spatial overlap of axons in M2 from different subtypes of NE or ACh neurons.

Noradrenergic system promotes switching and exploratory behavior

After photostimulation of frontal cortical NE axons, animals increased tendency to switch their choice during both matching pennies and a simple choice task. Our results echo the central conclusion

of an earlier study that used chemogenetics to activate LC inputs into the anterior cingulate cortex in rats, which increased behavioral variability (*63*), along with several other studies manipulating NE release (*99*–*101*). However, unlike the earlier work, in our task, there is no incentive to switch in the simple choice task, suggesting that this causally evoked behavioral change was not adaptive for improving performance. A recent study has shown that silencing the mouse anterior cingulate cortex decreases stochasticity in a foraging task (*102*), suggesting that the impact of frontal cortical NE on exploratory behavior may be bidirectional, in agreement with a theoretical proposal that NE may relate to the inverse temperature parameter in reinforcement learning (*25*). We interpret the increased probability to switch as a higher level of exploration; however, the behavior may also be viewed as consistent with a role of cortical NE in state formation and reset (*23*).

One may ask: Given the prominent task-related ACh transients, why was it that stimulating the cholinergic axons yielded no detectable change in behavior? This can be due to technical limitations because photostimulation was applied broadly to entire brain regions. We cannot recapitulate the precise fine-scale spatiotemporal patterns observed for the neuromodulatory transients. Unlike NE, we show that ACh transients are staggered with varying peak times at different locations, which could not be mimicked by wide-field optogenetic stimulation. Moreover, ACh and the medial frontal cortex have roles in decision-making and learning that are not captured by the behavioral tasks in this study. ACh contributes to cue-guided responses (*12*) and working memory (*11*). Furthermore, the medial frontal cortex including specifically neighboring region of the anterior cingulate cortex is involved in tracking volatility and uncertainty (*103*), as well as risk aversion (*104*) and belief or strategy updating (*105*–*107*). These are aspects of decision-making that are not emphasized in matching pennies, which may be why optogenetic stimulation of cholinergic axons in M2 yielded a null effect.

NE and ACh are major neurotransmitters in the brain. Here, taking advantage of novel fluorescent sensors and in vivo two-photon microscopy, we characterized noradrenergic and cholinergic signaling in subcellular resolution in M2 in mice while they were engaging in a competitive decision-making game. We uncovered that decision-related events are associated with NE and ACh transients with distinct spatiotemporal dynamics. Causal manipulation of frontal cortical NE heightened exploratory behavior. Our study contributes to the emerging understanding of the functions of these neuromodulators in value-based decision-making and provides clues into why their dysfunction may underlie cognitive symptoms of neuropsychiatric disorders.

MATERIALS AND METHODS

Animals

All animal procedures were conducted in accordance with procedures approved by the Institutional Animal Care and Use Committees at Yale University (animal use protocol no. 2019-11575) and Cornell University (animal use protocol no. 2021-0100). For imaging, adult male C57BL/6J mice were used (postnatal day 56 or older; no. 000664, the Jackson Laboratory). For photostimulation, adult male and female Dbh-Cre;Ai32 and ChAT-Cre;Ai32 mice were used (postnatal day 42 or older). Dbh-Cre;Ai32 mice were generated by crossing B6.Cg-*Dbh*$^{tm3.2(cre)Pjen}$/J (*75*) and B6.Cg-*Gt(ROSA)26Sor*$^{tm32(CAG-COP4*H134R/EYFP)Hze}$/J (no. 024109, the Jackson Laboratory) (*76*). ChAT-Cre;Ai32 mice were generated by crossing B6.129S-*Chat*$^{tm1(cre)Lowl}$/MwarJ (no. 031661, the Jackson Laboratory) (*77*) and B6.Cg-*Gt(ROSA)26Sor*$^{tm32(CAG-COP4*H134R/EYFP)Hze}$/J (no. 024109, the Jackson Laboratory). Mice were housed in groups of three to five animals with 12-hour/12-hour light/dark cycle control (lights off at 7 p.m.).

Surgical procedures

To prepare for imaging, animals underwent surgery for viral injection and cranial window implant. At the start of surgery, the animal was anesthetized with 2% isoflurane, which was reduced to 1 to 1.2% as the surgery progressed. The mouse was placed on a water-circulating heating pad (TP-700, Gaymar Stryker) in a stereotaxic frame (David Kopf Instruments). After injecting carprofen [5 mg/kg, subcutaneously (sc); no. 024751, Butler Animal Health] and dexamethasone (3 mg/kg, IM; Dexaject SP, no. 002459, Henry Shein Animal Health), the scalp of the animal was removed to expose the skull, which was cleaned three times with 70% ethanol and povidone-iodine. For the first part of procedure, a custom-made stainless steel headplate was glued to the skull with transparent Metabond (C&B, Parkell Inc.). For the second part of procedure, a 3-mm-diameter craniotomy was made over the longitudinal fissure [centered on anterior-posterior (AP): + 1.5 mm, medial-lateral (ML): 0.0 mm relative to bregma] using a high-speed rotatory drill (K.1070; Foredom). The dura was left intact and irrigated frequently with artificial cerebrospinal fluid (5 mM KCl, 5 mM Hepes, 135 mM NaCl, 1 mM $MgCl_2$, and 1.8 mM $CaCl_2$; pH 7.3) over the remainder of the procedure. The injection sites were located on the four vertices of a square with 0.2 mm in side length, centered on a medial target within M2 (AP + 1.5 mm, ML ± 0.5 mm relative to bregma). Either AAV9-CaMKII-$GRAB_{ACh3.0}$ or AAV9-hSyn-$GRAB_{NE2h}$ (titer > 10^{13} GC/ml, WZ Biosciences Inc.) was infused at the four-injection site through a glass micropipette attached to a microinjection unit (Nanoject II; Drummond). Each site was injected eight times with 4.6 nl of the aforementioned viruses over 2 min, at a depth of 0.4 mm from the dura. To minimize backflow of the injected solution, the micropipette was left in place for 5 min after each infusion. The cranial window consisted of one piece of 4-mm-diameter, #1 thickness prefabricated glass coverslip (no. 64-0720-CS-4R; Warner Instruments) and three pieces of 3-mm-diameter, #1 thickness prefabricated glass coverslips (no. 64-0720-CS-3R; Warner Instruments), glued together concentrically with ultraviolet-activated optical adhesive (NOA 61; Norland Products Inc.). The window was placed on the cortical surface with the glass plug facing down with gentle downward pressure provided by a wooden stick attached to the stereotaxic frame. The window was then secured by cyanoacrylate glue and Metabond. Postoperative analgesia (carprofen, 5 mg/kg, sc) was provided immediately and for three consecutive days following surgery. For most animals, the first and second parts of procedure were done in the same surgery, prior to behavioral training and imaging. We were concerned that this sequence prolongs the time of viral-mediated expression which may affect the signal. Therefore, for a few animals, the first and second parts of the procedure were done in separate surgeries, each with its own set of pre- and postoperative steps. The initial headplate implant allowed for training, and then once the animals were proficient, we injected viruses and prepared cranial window for imaging. We did not detect differences in the two approaches and therefore present only the combined dataset.

For experiments on the effects of NE transporter (NET) blockade on the $GRAB_{NE2h}$ signal, surgical procedures were detailed

previously (*108*). Briefly, ~478.4 nl of AAV9-hSyn-GRAB$_{NE2h}$ (titer > 10^{12} GC/ml, WZ Biosciences Inc.) was infused in the prelimbic cortex (centered on AP: +1.7 mm, ML: +0.3 mm relative to bregma, at a depth of 1.3 mm below the dura). Three weeks after viral injection, a second procedure was done to implant a gradient refractive index (GRIN) lens (Inscopix; cylindrical lens with 1.5 mm in length and 0.5 mm in diameter, working distance: ~0.1 mm). For lens implantation, a 0.5-mm-diameter craniotomy was remade over the previous viral injection site and the GRIN lens was implanted to a depth 0.1 mm dorsal to the viral injection target (i.e., 1.2 mm below dura). To prepare the cortex overlying the target region for mass effect due to the GRIN lens size, a sterile 30-gauge syringe was lowered to the implant's target position at a rate of 0.1 mm/min and then kept in position for 30 min and slowly retracted. The GRIN lens was then lowered to the target implant location at a rate of 0.1 mm/min. The GRIN lens collar was secured to the skull surface using cyanoacrylate glue. After the adhesive cured, a headplate was secured to the skull using Metabond. Pre- and postoperative were provided in the same way as described above.

To prepare for photostimulation, the steps closely followed procedures described previously (*109*). At the start of surgery, the animal was anesthetized with 2% isoflurane, which was reduced to 1 to 1.2% as the surgery progressed. The mouse was placed on a water-circulating heating pad (TP-700, Gaymar Stryker) in a stereotaxic frame (David Kopf Instruments). After injecting carprofen (5 mg/kg, sc; no. 024751, Butler Animal Health) and dexamethasone (3 mg/kg, sc; Dexaject SP, no. 002459, Henry Shein Animal Health), the scalp of the animal was removed to expose the skull, which was cleaned three times with 70% ethanol and povidone-iodine. After removing the scalp, the skull was lightly polished using acrylic polish kit (S23-0735, Pearson Dental) to remove residual tissue. A custom-made stainless steel headplate (eMachineShop) was glued onto the skull with Vetbond and the center well filled with transparent Metabond (one scoop of purple powder, seven drops of base, and two drops of catalyst; C&B, Parkell) to obtain a ~1- to 2-mm–thick layer. After waiting for about 20 min for the Metabond to cure, the surface of the Metabond layer was polished with progressively finer bits from the acrylic polish kit. After polishing, the well was covered with a very thin layer of clear nail polish (72180, Electron Microscopy Services) and allowed to dry fully. Postoperative analgesia (carprofen, 5 mg/kg, sc) was provided immediately and for three consecutive days following surgery. Animals were implanted with this clear skull cap for at least 2 weeks before the start of behavioral training.

Behavioral setup

The same training apparatus was used in our prior studies (*59*, *110*). Detailed instruction to construct the apparatus is available at https://github.com/Kwan-Lab/behavioral-rigs. Briefly, the mouse with a headplate implant was head fixed to a stainless steel holder (eMachineShop). The animal, restrained by an acrylic tube (8486K433; McMaster-Carr), was able to adjust its posture with limited gross movements. Two lick spouts made of blunted 20-gauge stainless steel needles were positioned in front of the subject near its mouth. The animal indicated its choice by licking the spout with its tongue. The contact with the lick spout formed a closed loop with wires that were soldered onto the spout and a battery-powered lick detection electronic circuit, which generated an output electrical signal. A computer received the signal via a data acquisition unit (USB-201, Measurement Computing) and logged it with the Presentation software (Neurobehavioral Systems). Two solenoid fluid valves (MB202-V-A-3–0-L-204; Gems Sensors & Controls) controlled the water delivery from the two lick ports independently. The amount of water was calibrated to ~4 μl per delivery by adjusting the duration of the electrical pulse sent by the Presentation software through a second data acquisition unit (USB-201, Measurement Computing). The sound cue signaling the trial start was played by two speakers (S120, Logitech) placed in front of the mouse. The whole setup was placed inside an audiovisual cart with walls covered by soundproof acoustic foams (5692T49, McMaster-Carr).

Two-photon imaging

The behavioral setup described above was placed under the two-photon microscope. The two-photon microscope (Movable Objective Microscope, Sutter Instrument) was controlled using ScanImage software 5.1. The excitation source was a Ti:sapphire femtosecond laser (Chameleon Ultra II, Coherent). Laser intensity was controlled by a Pockels cell (350-80-LA-02, Conoptics) and an optical shatter (LS6ZM2; Uniblitz/Vincent Associates). The beam was focused onto the sample with a 20×, numerical aperture 1.00 water immersion objective (N20X-PFH, Thorlabs via Olympus). The time-averaged excitation laser intensity was 120 to 180 mW after the objective. To image fluorescence transients from GRAB$_{NE2h}$ or GRAB$_{ACh3.0}$ sensors, excitation wavelength was set at 920 nm and emission was collected from 475 to 550 nm with a GaAsP photomultiplier tube. The subset of imaging experiments examining the effect of NE reuptake inhibitor on GRAB$_{NE2h}$ signals was done using the same two-photon microscope but with some differences in imaging conditions including, most notably, a different excitation wavelength of 980 nm as detailed in a different study previously (*108*). Time-lapse images were acquired at a resolution of 256 pixels by 256 pixels and a frame rate of 30.03 Hz using bidirectional scanning with resonant scanners. To synchronize behavioral and imaging data, a TTL pulse was sent by the Presentation software at the beginning of each trial from the USB-201 board of the behavioral system that controlled the water valves. The imaging system used the TTL pulse as an external trigger to initiate the imaging acquisition.

Photostimulation

The photostimulation apparatus had a design based on an earlier work (*109*) and is the exact same configuration used in a previous study (*106*). Briefly, a 473-nm fiber-coupled laser (473 nm, 75 mW; Obis LX, Coherent) was controlled by a pulse sequence generator (Pulse Pal, Sanworks). The fiber output was directed to a galvanometer-galvanometer scanner (6210H, Cambridge Technologies), which were driven by power supplies (SPD-3606, Cole-Parmer) and installed in a 60-mm cage system (Thorlabs). The excitation beam then passes through an F-theta scan lens (f = 160 mm; FTH160-1064-M39, Thorlabs) and is directed onto the animal's head. Calibration of the laser beam's position relative to bregma is achieved by visualizing the cortical surface using a monochromatic camera (Grasshopper3; GS3-U3-23S6M-C, Point Grey) with a telecentric lens (TEC-55, Computar). A blue light-emitting diode (LED) (470 nm) aimed at the animal's head was used as a masking light. Control of the laser, scanner, camera, and LED was executed through a data acquisition board (PCIe-6343, National Instruments) using custom software written in MATLAB (Mathworks). The behavior setup described above was placed under the photostimulation apparatus. The entire system is housed inside a custom T-slot frame box (80/22 LLC), shielded with

soundproof foam panels, on a vibration isolation table (CleanTop 781-651-02R, TMC).

Matching pennies

Animals were trained to play the matching pennies game with a component opponent (*59*). All procedures were written using the programming language in the Presentation software. The animals were fluid restricted with water provided during the daily behavioral session. On the days when the subjects were not trained (typically 1 day per week), a water bottle was placed in the home cage, allowing for ad libitum water access for 5 min.

Animals were trained in three phases. For phase 1 (2 days), the animals were habituated to the behavior apparatus. They may lick either spout for water. A water reward would be delivered after every lick at the corresponding spout with a minimal time interval of 1 s. The session would terminate after the animal collected 100 rewards. For phase 2 (~4 weeks), the animals were trained to follow the trial structure and withhold impulsive licks before the trial started. In each trial, a 5-kHz sound cue lasting for 0.2 s signaled the start of the trial. Then, the animal was given a 2-s window to lick either port. The 2-s response window would give a naïve mouse more time to act when they had not learnt the trial timing, therefore helping the animals to acquire the task faster. Once the first lick was detected, the 2-s response window would be terminated immediately. A water reward would be presented at the corresponding spout, following which a fixed 3-s period was presented for the animal to collect the reward. In the trials when the animal did not lick, the 3-s interval was still presented in full. A random ITI began after the 3-s consumption window. A number was drawn from a truncated exponential distribution with lambda = 0.333 and boundaries of 1 and 5, which was used as the duration of the ITI in seconds. If one or more licks were detected during the ITI, an additional ITI with duration redrawn from the same distribution would be appended to the end of current ITI, with a maximum of 5 ITIs. After the ITIs ended, the next trial would begin. The animal would be advanced into phase 3 to play the matching pennies game when the average number of ITI draws per trial was lower than 1.2 for three consecutive sessions. In phase 3 (~4 weeks), the animals were trained to play the matching pennies game against a computer opponent whose behavior was controlled by a script written in the programming language of the Presentation software. The trial timing is the same as phase 2: each trial begins with a 5-kHz, 0.2-s sound cue. Within a 2-s response window, the animal indicated its choice by licking either the left or right spout. A water reward would be delivered in the corresponding spout if the animal chose the same choice as the computer. Otherwise, there would be no reward. The computer opponent was programmed to provide competitive pressure in a way the same as "algorithm 2" described in previous studies (*59*, *60*, *111*). Specifically, the computer opponent kept a record of all the animal's past choices and outcomes within the current session and ran nine binomial tests on the conditional probability of the animal choosing left given the sequence of previous N choices ($N = 0$ to 4) and previous M choices and outcomes ($M = 1$ to 4), against the null hypotheses that the conditional probabilities of the animal choosing left was 0.5. If at least one of the tests rejected the null hypotheses with alpha < 0.05, the computer then chose right with the significant conditional probability that was most biased from 0.5. If none of the null hypothesis was rejected, the computer randomly generated either choice with equal probabilities. The animal could play for as many trials as it desires, and a session would terminate when no response was detected for 10 consecutive trials. Mice reached stable performance when they played matching pennies for three consecutive sessions with a minimum of 40% reward rate. Specifically, in the ACh group, five mice spent a range of 6 to 14 sessions, and in the NE group, four mice spent 5 to 10 sessions in phase 3 training until reaching criterion.

Initially, mice were trained in dedicated behavioral setups. After reaching criterion, animals were trained to play the same matching pennies game in the behavioral setup within the two-photon imaging or photostimulation rig. They would be deemed to have adapted when mice played matching pennies for three consecutive sessions with a minimum of 40% reward rate, which was when imaging or photostimulation experiments would commence.

Matching pennies and photostimulation

During matching pennies, for photostimulation trials, laser was turned on for photostimulation (frequency: 40 Hz; pulse duration: 0.1 ms) from onset of cue to 1 s after choice was made (i.e., first lick within response window). The stimulation schedule was determined based on previous researches with 40-Hz stimulation on noradrenergic and cholinergic terminals (*112*–*114*). Photostimulation was applied to one of four possible locations: left secondary motor cortex (M2-L; +1.5 mm AP, −0.3 mm ML from bregma), right secondary motor cortex (M2-R; +1.5, +0.3), left primary visual cortex (V1-L; −3.0, −2.0), or right primary visual cortex (V1-R; −3.0, +2.0). For all trials, including photostimulation and control (without photostimulation) trials, the masking blue LED would be turned on from onset of cue to 1 s after choice was made. For the "varying power" paradigm, photostimulation occurred on 40% of the trials randomly with 10% allocated to each region (M2-L, M2-R, V1-L, and V1-R). One power was used for a session, but power changed across sessions in a pseudorandom order between 0, 1.5, and 3 mW. For 0 mW, the laser was powered as usual but in standby mode such that there was no laser emission. For the "varying region" paradigm, photostimulation occurred on 10% of the trials at 3 mW. One region was tested for a session, but region changed across sessions in a pseudorandom order between M2-L, M2-R, V1-L, and V1-R.

Simple choice task

Each trial begins with a 5-kHz, 0.2-s sound cue. Within a 2-s response window, the animal indicated its choice by licking either the left or right spout. In trial type 1, the left spout has 50% chance of delivering water and photostimulation (from choice to 1 s after choice was made) whereas the right spout has 50% chance of delivering only water. In trial type 2, the left spout has 50% chance of delivering only water whereas the right spout has 50% chance of delivering photostimulation and water. To determine whether the animal would bias its choice if one of the choices would lead to photostimulation, the latter was delivered immediately after the choice, slightly different from the matching pennies game. A session begins with a first trial of trial type 1 or 2 randomly. The next trial has a 1/11 probability to switch trial type. There were no external stimuli beyond the probabilistic photostimulation and water delivery to inform the mouse of the trial type switch. The animal could play for as many trials as it desires, and a session would terminate when no response was detected for 20 consecutive trials.

Pupillometry

A monochrome camera (GigE G3-GM11-M1920, Dalsa) with a 55-mm telecentric lens (TEC-55, Computar) was aimed at the eye of

the animal contralateral to the hemisphere where imaging was performed. Video was acquired at 20 Hz. The computer running the Presentation software sent TTL pulses every 30 s to another computer controlling the camera through a USB data acquisition device (USB-201; Measurement Computing). The timestamp of the TTL pulse was logged by MATLAB 2019b (MathWorks) with a custom script, such that the video could be aligned to behavioral events post hoc. The computer running the Presentation software sent TTL pulses every 30 s to the two-photon microscope to trigger imaging. Each session lasted 30 min. Animals were tested either naïve or after going through the entire behavioral training protocol for matching pennies.

Auditory evoked responses

This measurement relied on the same behavioral setup as the matching pennies. A 4-kHz, 50-ms auditory stimulus was played at the beginning of each trial. A random ITI was presented following the stimulus. The duration of the ITI in seconds was drawn from a continuous uniform distribution with boundaries of 1 and 4. The next trial would begin after the ITI. Each session lasted 200 trials.

NE reuptake inhibitor

To test how extracellular accumulation of NE affects the $GRAB_{NE2h}$ signal, male C57BL/6J mice ($n = 3$) were treated with the NET blocker desipramine [10 mg/kg, intraperitoneally (ip)] or saline 20 min before an imaging session. The treatment order was counterbalanced across mice.

Histology

Following imaging experiments, mice were transcardially perfused with chilled phosphate-buffered saline (PBS) followed by formaldehyde solution (4% in PBS). The brains were then fixed in 4% formaldehyde solution for 1 hour before they were transferred to 30% sucrose solution at 4°C. After about 24 hours, the brains were cut into 50-μm-thick coronal sections with a vibratome (VT 1000S, Leica). The brain sections were washed three times with PBS solution before being immersed with chicken anti–green fluorescent protein (GFP) antibody (1:500; ab13970, Abcam) for 12 hours at 4°C. Then, Alexa Fluor 488–conjugated goat anti-chicken secondary antibody (1:50; ab209487, Abcam) was used to label the primary antibody for 3 hours at room temperature. The sections were then mounted with DPX and imaged with an inverted wide-field fluorescence microscope.

Following photostimulation experiments, mice were transcardially perfused with chilled PBS then formaldehyde solution (4% in PBS). The brains were fixed in 4% formaldehyde solution for 24 hours at 4°C before being transferred to PBS. Then, brains were processed using the vibratome into 30-μm-thick coronal sections. Sections were washed five times with PBS and incubated in PBS with 0.3% Triton X-100 (PBST) for 20 min at room temperature. Slices were blocked with 10% normal goat serum in PBST for 1 hour at room temperature followed by incubation with primary anti-GFP antibody (1:200, ab290, Abcam) in 10% normal goat serum in PBST at 4°C overnight. Sections were washed three times in PBS then incubated with Alexa Fluor 488–conjugated goat anti-rabbit secondary antibody (1:500; ab150077, Abcam) for 2 hours at room temperature. Slices were mounted with Vectashield Antifade Mounting Medium with DAPI (H-1200-10, VectorLabs) and imaged with a Zeiss LSM 710 confocal microscope.

Preprocessing of matching pennies data

To quantify the randomness in the animals' choices, the three-choice entropy of the choice sequence is calculated by

$$\text{Entropy} = -\sum_k p_k \log_2 p_k$$

where p_k is the frequency of occurrence of a three-choice pattern in a session. Because there were two options to choose from, there were $2^3 = 8$ potential patterns possible (e.g., left-left-left, left-left-right, left-right-left, etc.). The maximum value for entropy is 3 bits. For matching pennies, the animals tended to select the same option for around 30 trials toward the end of each session. The three-choice entropy over a moving 30-trial window was calculated for each session, and the MATLAB function ischange was used to fit with a piecewise linear function. The trials after the fitted curve fell below a value of 1 were discarded to exclude the repetitive trials in the analyses. In cases where the curve recovered to a value greater than 1 after it dropped below 1, or if it never fell below a value of 1, the entire session was used for analysis.

Preprocessing of pupillometry data

The preprocessing of pupillometry data was similar to a previous work (*59*). To extract the diameters of the pupil from the video recordings, we used DeepLabCut (DLC) 2.0 (*115*, *116*). Five labels including the central, uppermost, leftmost, lowermost, and rightmost points of the pupil were manually labeled by the experimenter on a small subset of the video frames. The annotated frames were used to train DLC to automatically label the 5 points on the remainder of the video. The absolute pupil diameter was calculated by taking the distance between the leftmost and rightmost labels. The other labels were not considered because we found that the labeling of the lowermost points was interfered by the lower eyelid, resulting in an inaccurate estimation. The absolute pupil diameter was passed through a 4-Hz low-pass filter with the MATLAB function lowpass. Using the MATLAB function isoutlier, we detected and deleted any data points that were greater than 3 scaled median absolute deviation (MAD) from the median. The baseline of the signal was computed with a 10-min moving window, which was used to convert the signal to *z*-score to account for drift over a session.

Preprocessing of imaging data

Time-lapse images were processed for *x*-*y* motion correction using customized MATLAB scripts based on NoRMCorre (*117*). The FOV spans 142.66 μm by 142.66 μm, or 256 pixels by 256 pixels. For analysis, we only use the 124.83 μm by 124.83 μm, or 224 pixels by 224 pixels, portion at the center of the FOV to avoid artifacts near the FOV edges due to motion correction processing. The analyzed region was divided into 28 by 28 grids. Each grid was a 4.46 μm by 4.46 μm, or 8 pixels by 8 pixels, square, which was considered as an ROI. We decided to use grids to subdivide the FOV as an unbiased way to analyze spatial dependence rather than neural morphology because the $GRAB_{NE2h}$ and $GRAB_{ACh3.0}$ sensors labeled primarily neuropils that are indistinct for manual drawing of ROIs. For each ROI, the fractional change in fluorescence, $\Delta F/F(t)$, was calculated as

$$\frac{\Delta F}{F}(t) = \frac{F(t) - F_0(t)}{F_0(t)}$$

where $F_0(t)$ is the baseline fluorescence as a function of time, which was the 10th percentile of the fluorescent intensity within a 2-min running window centered at time t.

Analysis of behavioral data—Computational models

To quantify the choice behavior, we adopted a Q-learning with forgetting model plus choice kernels (FQ_RPE_CK) (*59*). On trial n, for a choice c_n that leads to an outcome r_n, the action value Q_n^i associated with an action i is updated by

$$Q_{n+1}^i = \begin{cases} Q_n^i + \alpha\left(r_n - Q_n^i\right) & \text{if } c_n = i \\ (1-\alpha)Q_n^i & \text{if } c_n \neq i \end{cases}$$

where α is the learning rate, and the forgetting rate for the unchosen action. In our task, there are two options, so $i \in \{L, R\}$. For the outcome, $r_n = 1$ for reward, 0 for no reward. Moreover, to capture the animal's tendency to make decisions based purely on previous choices, there are choice kernels K_n^i updated by

$$K_{n+1}^i = \begin{cases} K_n^i + \alpha_K\left(1 - K_n^i\right) & \text{if } c_n = i \\ \left(1-\alpha_K\right)K_n^i & \text{if } c_n \neq i \end{cases}$$

where α_K is the learning rate of the choice kernel. For action selection, the probability to choose action i on trial n is given by a softmax function

$$P\left(c_n = i\right) = \frac{\exp\left(\beta Q_n^i + \beta_K K_n^i\right)}{\sum_j \exp\left(\beta Q_n^j + \beta_K K_n^j\right)}$$

where β and β_K are the inverse temperature parameters for action values and choice kernels, respectively.

To fit the computational models to the behavioral data, for each subject, the sequence of choices and outcomes were concatenated across sessions. Each model was fitted to the data using a maximum-likelihood algorithm implemented with the fmincon function in MATLAB, with the constraints $0 \leq \alpha, \alpha_K, \alpha_R, \alpha_U \leq 1$, and$0 < \beta, \beta_K$. These fits also yielded latent decision variables such as action values and choice kernels that would be used for the subsequent multiple linear regression analyses.

Analysis of imaging data—Peristimulus time histogram

To obtain trial-averaged activity traces [peristimulus time histogram (PSTH)] aligned to the cue onset for different trial types, we first aligned $\Delta F/F(t)$ traces based on their timing relative to the cue onset of the corresponding trials and then took the mean across traces. We then estimated the average and 95% confidence interval over mean traces of all recorded ROIs with bootstrapping procedure to get the average PSTH for a single session.

Analysis of imaging data—Linear regression

To determine how fluorescence signals may relate to task-related variables such as choices and outcomes, we used a multiple linear regression equation adapted from our previous study (*59*)

$$\begin{aligned} \frac{\Delta F}{F}(t) = {} & b_0 + b_1 c_{n+1} + b_2 r_{n+1} + b_3 c_{n+1} r_{n+1} \\ & + b_4 c_n + b_5 r_n + b_6 c_n r_n \\ & + b_7 c_{n-1} + b_8 r_{n-1} + b_9 c_{n-1} r_{n-1} \\ & + b_{10} c_{n-2} + b_{11} r_{n-2} + b_{12} c_{n-2} r_{n-2} \\ & + b_{13} \overline{r_n^{\mathrm{MA}}} + b_{14} r_n^{\mathrm{Cum.}} + \varepsilon(t) \end{aligned}$$

where $\frac{\Delta F}{F}(t)$ is the fractional changes in fluorescence at time t in trial n; $c_{n+1}, c_n, c_{n-1}, c_{n-2}$ are the choices made on the next trial, the current trial; the previous trial, and the trial before the previous trial, respectively; $r_{n+1}, r_n, r_{n-1}, r_{n-2}$ are the outcomes for the next trial, the current trial, the previous trial, and the trial before the previous trial, respectively; $b_0, \ldots, b_{14}$ are the regression coefficients; and $\varepsilon(t)$ is the error term. Choices were dummy coded as 0 for ipsilateral responses and 1 for contralateral responses. Outcomes were dummy coded as 0 for no reward and 1 for reward. For the last two predictors, $\overline{r_n^{\mathrm{MA}}}$ is the average reward over the previous 20 trials, given by the equation

$$\overline{r_n^{\mathrm{MA}}} = \frac{\sum_{i=0}^{19} r_{n-i}}{20}$$

Also, $r_n^{\mathrm{Cum.}}$ is the normalized cumulative reward during the session, calculated by

$$r_n^{\mathrm{Cum.}} = \frac{\sum_{i=1}^{n} r_i}{\sum_{i=1}^{N} r_i}$$

where n denotes the current trial number and N is the total number of trials in the session.

To examine the modulation effect of lick rate on fluorescence signals, we constructed a multiple linear regression

$$\begin{aligned} \frac{\Delta F}{F}(t) = {} & b_0 + b_1 c_{n+1} + b_2 r_{n+1} + b_3 c_{n+1} r_{n+1} \\ & + b_4 c_n + b_5 r_n + b_6 c_n r_n \\ & + b_7 c_{n-1} + b_8 r_{n-1} + b_9 c_{n-1} r_{n-1} \\ & + b_{10} c_{n-2} + b_{11} r_{n-2} + b_{12} c_{n-2} r_{n-2} \\ & + b_{13} \overline{r_n^{\mathrm{MA}}} + b_{14} r_n^{\mathrm{Cum.}} + b_{15} lick(t) + \varepsilon(t) \end{aligned}$$

where $lick(t)$ is the number of licks at time t.

To determine how fluorescence signals may relate to switch behavior, we used multiple linear regression

$$\frac{\Delta F}{F}(t) = b_0 + b_1 s_n + b_2 r_n + b_3 s_n r_n + b_4 \overline{r_n^{\mathrm{MA}}} + b_5 r_n^{\mathrm{Cum.}} + \varepsilon(t)$$

where s_n denotes the switch factor made on the current trial, and $b_0, \ldots, b_5$ are the regression coefficients. Switches were dummy coded as 0 for a stay choice (same choice made on the current trial as the previous one), 1 for a contralateral switch (an ipsilateral choice

made on the previous trial to a contralateral choice made on the current trial), and −1 for an ipsilateral switch (a contralateral choice made on the previous trial to an ipsilateral switch made on the current trial). We did not include switch and outcome for past or future trials as predictors because these variables are highly correlated.

To determine how fluorescence signals may relate to latent decision variables for action selection, we used multiple linear regression

$$\begin{aligned}\frac{\Delta F}{F}(t) = {} & b_0 + b_1 c_n + b_2 r_n + b_3 c_n r_n \\ & + b_4 c_{n-1} + b_5 r_{n-1} + b_6 c_{n-1} r_{n-1} \\ & + b_7\left(Q_n^{\mathrm{L}} - Q_n^{\mathrm{R}}\right) + b_8 Q_n^{\mathrm{chosen}} \\ & + b_9\left(K_n^{\mathrm{L}} - K_n^{\mathrm{R}}\right) + b_{10} K_n^{\mathrm{chosen}} \\ & + b_{11}\overline{r_n^{\mathrm{MA}}} + b_{12} r_n^{\mathrm{Cum.}} + \varepsilon(t)\end{aligned}$$

where Q_n^{L} and Q_n^{R} denote the action values of the left and right choices in trial n, respectively; Q_n^{chosen} is the value of the action chosen in trial n; K_n^{L} and K_n^{R} are the choice kernels of the left and right choices in trial n, respectively; and K_n^{chosen} is the choice kernel of the action chosen in trial n.

To determine how fluorescence signals may relate to latent decision variables for value updating, we used multiple linear regression

$$\frac{\Delta F}{F}(t) = b_0 + b_1 c_n + b_2 c_{n-1} + b_3 r_{n-1} + b_4\left(Q_n^{\mathrm{L}} - Q_n^{\mathrm{R}}\right) + b_5\left(r_n - Q_n^{\mathrm{chosen}}\right) + \varepsilon(t)$$

where $r_n - Q_n^{\mathrm{chosen}}$ is the positive or negative RPE for $r_n = 1$ or $r_n = 0$, respectively.

For each session, the regression coefficients were determined by fitting the equations to data using the MATLAB function fitlm. The fit was done in 100-ms time bins that span from −3 to 5 s relative to cue onset, using mean $\Delta F/F$ within the time bins. For a given predictor and an ROI, if the regression coefficients were significant ($P < 0.01$) for at least three consecutive or 10 total time points between −3 and 5 s from cue onset, the ROI was considered significantly modulated by the predictor. The time span was chosen so that it included the long-lasting effect of choice and outcome encoding without encroaching into the next trial. To summarize the results, for each predictor, we calculated the proportion of ROIs in which the regression coefficient was significantly different from zero ($P < 0.01$). To determine whether the proportion was significantly different from chance, we performed a chi-square test against the null hypothesis that there was a 1% probability that a given predictor was mischaracterized as significant by chance in a single session.

Analysis of imaging data—Hierarchical clustering

To analyze the degree of similarity in task-related activity across ROIs, within each session, we applied hierarchical clustering on the regression coefficients for the current outcome for the ROIs that were significantly modulated by the current outcome. We clustered the ROIs within each session into two clusters based on the cross-correlation of the regression coefficients within −3 to 5 s from cue using the MATLAB function clusterdata. The optimal number of clusters was validated with silhouette analysis. Note that the clusterdata function would always cluster any given dataset into two clusters, yet in some sessions, the data were better fitted with only one cluster. Therefore, we identified two distinct groups post hoc based on the direction of modulation and then placed every cluster identified by clusterdata into either of these two groups as follows: First, we calculated the mean coefficients as a function of time of each cluster over different ROIs; we then calculated the area under the curve of the average coefficients between 0 and 2 s from cue. Clusters with a positive area under the curve were considered group 1, and clusters with a negative area under the curve were considered group 2. Once all the ROIs from all sessions were categorized into either group, we then identified the ROIs that were significantly modulated by current choice and/or current reinforcer (choice-outcome interaction) within the groups (fig. S6). For visualization, the ROIs were sorted by the center of mass of the regression coefficients for the current outcome. The hierarchical clustering procedures described above were performed for $\mathrm{GRAB}_{\mathrm{NE2h}}$ and $\mathrm{GRAB}_{\mathrm{ACh3.0}}$ data separately.

Analysis of imaging data—Temporal dynamics of the task-related activity

To quantify the temporal dynamics of the task-related activity, the time-to-peak value was calculated for each ROI as the duration from cue onset time to the peak coefficient time (the time when the regression coefficient reached the maximum magnitude). Afterward, the median and variance of time-to-peak and the median of peak-value were taken for each session. This quantification was performed for different regression coefficients (e.g., choice, outcome, and reinforcer) separately.

Analysis of imaging data—Information encoding of single ROIs

To examine the spatial patterns of task-related activity, we calculated the average regression coefficients over time for the current choice, current outcome, and current reinforcer (choice-outcome interaction) separately for each session. We used the Pearson's chi-square test for independence to test whether the event that a given ROI was modulated by one predictor was independent from the event that the same ROI was modulated by another predictor.

To compare the level of information integration between $\mathrm{GRAB}_{\mathrm{NE2h}}$ and $\mathrm{GRAB}_{\mathrm{ACh3.0}}$ data, we calculated six conditional probabilities that an ROI is modulated by one variable (v_1) given that the same ROI is modulated by another variable v_2 for each session, given by the equation

$$Pr\left(v_1 \mid v_2\right) = \frac{N\left(v_1 \& v_2\right)}{N\left(v_2\right)}$$

where $N\left(v_1 \& v_2\right)$ denotes the number of ROIs that were modulated by v_1 and v_2; $N\left(v_2\right)$ denotes the number of ROIs that were modulated by v_2; and v_1 and v_2 can be either c_n, r_n, or x_n ($v_1 \neq v_2$). The median test was used to determine whether the conditional probabilities of an ROI was modulated by one predictor given the ROI was modulated by another predictor were significantly different between the $\mathrm{GRAB}_{\mathrm{NE2h}}$ and $\mathrm{GRAB}_{\mathrm{ACh3.0}}$ data because the median test is more robust with small sample size and less sensitive to asymmetry.

Analysis for auditory evoked responses

To obtain the mean auditory evoked responses, we first aligned the $\Delta F/F(t)$ based on the times of auditory stimulus onset and then calculated the PSTH over all 200 trials for each ROI. To examine the temporal dynamics of the auditory evoked response, the time-to-peak-$\Delta F/F$

value was calculated for each ROI as the duration from cue onset time to the peak-$\Delta F/F$ time (the time when the PSTH reached the highest value). The decay time was the decay constant obtained by fitting the PSTH from the peak time to the end of trial (3 s after the cue time) to single exponential decay. Afterward, the median of time-to-peak and decay time were taken for each session.

Analysis for pupillary fluctuation

For plotting example traces of fluorescent and pupil signals, we smoothed the $\Delta F/F(t)$ and pupil z-score traces using a Gaussian kernel with the MATLAB function smooth. To characterize the relationship between $\Delta F/F(t)$ and pupil z-score, we first determine the cross-correlation between $\Delta F/F(t)$ and pupil z-score from lag of −2 to 2 s for each ROI, then determine the maximum cross-correlation value within this lag range, and lastly tabulate a histogram for the maximum coefficients for all ROIs separately for $GRAB_{NE2h}$ and $GRAB_{ACh3.0}$ data.

Analysis of imaging data—Effect of NE reuptake inhibitor on $GRAB_{NE2h}$ dynamics

Time-lapse images acquired through the GRIN lens were corrected for x-y motion artifacts using NoRMCorre. For analysis, the first 30 s of imaging were discarded and regions of dense $GRAB_{NE2h}$ expression in the central 80% of the imaged FOV were manually traced as ROIs ($n = 51$ desipramine; $n = 59$ saline) using a custom graphical user interface in MATLAB. Each ROI's raw fluorescence trace was extracted as the pixel-wide mean within the ROI. The effect of NET blockade on the accumulation of extracellular NE was tested by comparing the initial 5 min of $GRAB_{NE2h}$ fluorescence (normalized within-ROI to the average fluorescence in the first 20 s) between treatment groups using two-sample t tests for each imaging frame (Bonferroni-corrected for multiple comparisons). Fluorescence signals were also compared using power spectral density and spatial coherence after the detrending and z-scoring each ROI's raw fluorescence trace. Power density was calculated following Fourier transform using the fft function in MATLAB. Local spatial coherence for each ROI and the bulk $GRAB_{NE2h}$ signal was calculated across the same frequencies using the magnitude squared coherence estimate from mscohere in MATLAB. Differences in power spectra and coherence between treatment groups were tested using Wilcoxon signed-rank tests for each 0.01-Hz bin between 0.001 and 15 Hz (Bonferroni-corrected for multiple comparisons).

Analysis for photostimulation

For the mouse's probability to switch on the next trial, a multivariate ANOVA was performed for each condition (ChAT-Cre;Ai32 or Dbh-Cre;Ai32) to determine the effect of region and power or stimulation. Tukey post hoc test was used as needed. For analyzing the mouse's probability to switch as a function of number of trials since last stimulation (trial n), the probability for the mouse to switch choices on the first trial following stimulation ($n + 1$), second trial after photostimulation ($n + 2$), and so on, was calculated. We used only the subset of trials in which no photostimulation occurred up to the trial of interest. For analyzing session-wide metrics such as entropy, number of trials completed, and reward rate, a one-way ANOVA was performed for each condition to determine the effect of power or region. Tukey post hoc test was used as needed. For the simple choice task, a t test was performed to compare sessions with and without stimulation (3 mW versus 0 mW) for each condition on metrics of number of responses/switches, probability of choosing side with stimulation, and probability of switching on the next trial.

Animal numbers

For two-photon imaging, the dataset for matching pennies included 47 sessions from five animals expressing $GRAB_{ACh3.0}$ and 38 sessions from four animals expressing $GRAB_{NE2h}$. Auditory evoked responses included seven sessions from five animals expressing $GRAB_{ACh3.0}$ and seven sessions from seven animals expressing $GRAB_{NE2h}$. Spontaneous pupil fluctuation included 10 sessions from five animals expressing $GRAB_{ACh3.0}$ and 7 sessions from seven animals expressing $GRAB_{NE2h}$. For photostimulation, the dataset came from seven ChAT-Cre;Ai32 and six Dbh-Cre;Ai32 mice. The varying power paradigm included 91 sessions from seven ChAT-Cre;Ai32 mice and 76 sessions from six Dbh-Cre;Ai32 mice. The varying region paradigm included 49 sessions from the same seven ChAT-Cre;Ai32 mice and 41 sessions from the same six Dbh-Cre;Ai32 mice. The simple choice task included 8 sessions from four ChAT-Cre;Ai32 mice and 12 sessions from six Dbh-Cre;Ai32.

Supplementary Materials

This PDF file includes:

Figs. S1 to S8
Tables S1 to S10

REFERENCES AND NOTES

1. M. R. Picciotto, M. J. Higley, Y. S. Mineur, Acetylcholine as a neuromodulator: Cholinergic signaling shapes nervous system function and behavior. *Neuron* **76**, 116–129 (2012).
2. B. J. Everitt, T. W. Robbins, Central cholinergic systems and cognition. *Annu. Rev. Psychol.* **48**, 649–684 (1997).
3. G. Aston-Jones, J. D. Cohen, An integrative theory of locus coeruleus-norepinephrine function: Adaptive gain and optimal performance. *Annu. Rev. Neurosci.* **28**, 403–450 (2005).
4. G. Buzsaki, R. G. Bickford, G. Ponomareff, L. J. Thal, R. Mandel, F. H. Gage, Nucleus basalis and thalamic control of neocortical activity in the freely moving rat. *J. Neurosci.* **8**, 4007–4026 (1988).
5. J. W. Dalley, J. McGaughy, M. T. O'Connell, R. N. Cardinal, L. Levita, T. W. Robbins, Distinct changes in cortical acetylcholine and noradrenaline efflux during contingent and noncontingent performance of a visual attentional task. *J. Neurosci.* **21**, 4908–4914 (2001).
6. A. J. Yu, P. Dayan, Acetylcholine in cortical inference. *Neural Netw.* **15**, 719–730 (2002).
7. J. L. Herrero, M. J. Roberts, L. S. Delicato, M. A. Gieselmann, P. Dayan, A. Thiele, Acetylcholine contributes through muscarinic receptors to attentional modulation in V1. *Nature* **454**, 1110–1114 (2008).
8. L. Pinto, M. J. Goard, D. Estandian, M. Xu, A. C. Kwan, S. H. Lee, T. C. Harrison, G. Feng, Y. Dan, Fast modulation of visual perception by basal forebrain cholinergic neurons. *Nat. Neurosci.* **16**, 1857–1863 (2013).
9. J. McGaughy, J. W. Dalley, C. H. Morrison, B. J. Everitt, T. W. Robbins, Selective behavioral and neurochemical effects of cholinergic lesions produced by intrabasalis infusions of 192 IgG-saporin on attentional performance in a five-choice serial reaction time task. *J. Neurosci.* **22**, 1905–1913 (2002).
10. V. Parikh, R. Kozak, V. Martinez, M. Sarter, Prefrontal acetylcholine release controls cue detection on multiple timescales. *Neuron* **56**, 141–154 (2007).
11. Y. Chudasama, J. W. Dalley, F. Nathwani, P. Bouger, T. W. Robbins, Cholinergic modulation of visual attention and working memory: Dissociable effects of basal forebrain 192-IgG-saporin lesions and intraprefrontal infusions of scopolamine. *Learn. Mem.* **11**, 78–86 (2004).
12. H. J. Gritton, W. M. Howe, C. S. Mallory, V. L. Hetrick, J. D. Berke, M. Sarter, Cortical cholinergic signaling controls the detection of cues. *Proc. Natl. Acad. Sci. U.S.A.* **113**, E1089–E1097 (2016).
13. M. Goard, Y. Dan, Basal forebrain activation enhances cortical coding of natural scenes. *Nat. Neurosci.* **12**, 1444–1449 (2009).
14. J. Zou, J. Willem de Gee, Z. Mridha, S. Trinh, A. Erskine, M. Jing, J. Yao, S. Walker, Y. Li, M. McGinley, S. A. Hires, Goal-directed motor actions drive acetylcholine dynamics in sensory cortex. *Elife* **13**, RP96931 (2024).

15. M. Jouvet, Biogenic amines and the states of sleep. *Science* **163**, 32–41 (1969).
16. D. A. McCormick, H. C. Pape, A. Williamson, Actions of norepinephrine in the cerebral cortex and thalamus: Implications for function of the central noradrenergic system. *Prog. Brain Res.* **88**, 293–305 (1991).
17. C. W. Berridge, B. D. Waterhouse, The locus coeruleus–noradrenergic system: Modulation of behavioral state and state-dependent cognitive processes. *Brain Res. Brain Res. Rev.* **42**, 33–84 (2003).
18. D. Servan-Schreiber, H. Printz, J. D. Cohen, A network model of catecholamine effects: Gain, signal-to-noise ratio, and behavior. *Science* **249**, 892–895 (1990).
19. E. Eldar, J. D. Cohen, Y. Niv, The effects of neural gain on attention and learning. *Nat. Neurosci.* **16**, 1146–1153 (2013).
20. G. Aston-Jones, J. Rajkowski, J. Cohen, Role of locus coeruleus in attention and behavioral flexibility. *Biol. Psychiatry* **46**, 1309–1320 (1999).
21. J. Reimer, M. J. McGinley, Y. Liu, C. Rodenkirch, Q. Wang, D. A. McCormick, A. S. Tolias, Pupil fluctuations track rapid changes in adrenergic and cholinergic activity in cortex. *Nat. Commun.* **7**, 13289 (2016).
22. M. E. Hasselmo, J. M. Bower, Acetylcholine and memory. *Trends Neurosci.* **16**, 218–222 (1993).
23. S. Bouret, S. J. Sara, Network reset: A simplified overarching theory of locus coeruleus noradrenaline function. *Trends Neurosci.* **28**, 574–582 (2005).
24. P. Dayan, A. J. Yu, Phasic norepinephrine: A neural interrupt signal for unexpected events. *Network* **17**, 335–350 (2006).
25. K. Doya, Metalearning and neuromodulation. *Neural Netw.* **15**, 495–506 (2002).
26. S. J. Sara, The locus coeruleus and noradrenergic modulation of cognition. *Nat. Rev. Neurosci.* **10**, 211–223 (2009).
27. A. J. Yu, P. Dayan, Uncertainty, neuromodulation, and attention. *Neuron* **46**, 681–692 (2005).
28. B. Hangya, S. P. Ranade, M. Lorenc, A. Kepecs, Central cholinergic neurons are rapidly recruited by reinforcement feedback. *Cell* **162**, 1155–1168 (2015).
29. S. C. Lin, M. A. Nicolelis, Neuronal ensemble bursting in the basal forebrain encodes salience irrespective of valence. *Neuron* **59**, 138–149 (2008).
30. C. H. Liu, J. E. Coleman, H. Davoudi, K. Zhang, M. G. Hussain Shuler, Selective activation of a putative reinforcement signal conditions cued interval timing in primary visual cortex. *Curr. Biol.* **25**, 1551–1561 (2015).
31. P. L. Croxson, D. A. Kyriazis, M. G. Baxter, Cholinergic modulation of a specific memory function of prefrontal cortex. *Nat. Neurosci.* **14**, 1510–1512 (2011).
32. A. Arnsten, P. S. Goldman-Rakic, α2-adrenergic mechanisms in prefrontal cortex associated with cognitive decline in aged nonhuman primates. *Science* **230**, 1273–1276 (1985).
33. A. F. Arnsten, M. J. Wang, C. D. Paspalas, Neuromodulation of thought: Flexibilities and vulnerabilities in prefrontal cortical network synapses. *Neuron* **76**, 223–239 (2012).
34. E. C. Clayton, J. Rajkowski, J. D. Cohen, G. Aston-Jones, Phasic activation of monkey locus ceruleus neurons by simple decisions in a forced-choice task. *J. Neurosci.* **24**, 9914–9920 (2004).
35. S. Bouret, B. J. Richmond, Sensitivity of locus ceruleus neurons to reward value for goal-directed actions. *J. Neurosci.* **35**, 4005–4014 (2015).
36. L. M. Teles-Grilo Ruivo, K. L. Baker, M. W. Conway, P. J. Kinsley, G. Gilmour, K. G. Phillips, J. T. R. Isaac, J. P. Lowry, J. R. Mellor, Coordinated acetylcholine release in prefrontal cortex and hippocampus is associated with arousal and reward on distinct timescales. *Cell Rep.* **18**, 905–917 (2017).
37. C. B. Saper, Organization of cerebral cortical afferent systems in the rat. II. Magnocellular basal nucleus. *J. Comp. Neurol.* **222**, 313–342 (1984).
38. J.-H. Kim, A.-H. Jung, D. Jeong, I. Choi, K. Kim, S. Shin, S. J. Kim, S.-H. Lee, Selectivity of neuromodulatory projections from the basal forebrain and locus ceruleus to primary sensory cortices. *J. Neurosci.* **36**, 5314–5327 (2016).
39. L. Zaborszky, A. Csordas, K. Mosca, J. Kim, M. R. Gielow, C. Vadasz, Z. Nadasdy, Neurons in the basal forebrain project to the cortex in a complex topographic organization that reflects corticocortical connectivity patterns: An experimental study based on retrograde tracing and 3D reconstruction. *Cereb. Cortex* **25**, 118–137 (2015).
40. S. Lohani, A. H. Moberly, H. Benisty, B. Landa, M. Jing, Y. Li, M. J. Higley, J. A. Cardin, Spatiotemporally heterogeneous coordination of cholinergic and neocortical activity. *Nat. Neurosci.* **25**, 1706–1713 (2022).
41. D. G. Amaral, H. M. Sinnamon, The locus coeruleus: Neurobiology of a central noradrenergic nucleus. *Prog. Neurobiol.* **9**, 147–196 (1977).
42. R. Moore, F. Bloom, Central catecholamine neuron systems: Anatomy and physiology of the norepinephrine and epinephrine systems. *Annu. Rev. Neurosci.* **2**, 113–168 (1979).
43. L. A. Schwarz, K. Miyamichi, X. J. Gao, K. T. Beier, B. Weissbourd, K. E. DeLoach, J. Ren, S. Ibanes, R. C. Malenka, E. J. Kremer, L. Luo, Viral-genetic tracing of the input-output organization of a central noradrenaline circuit. *Nature* **524**, 88–92 (2015).
44. S. E. Loughlin, S. L. Foote, J. H. Fallon, Locus coeruleus projections to cortex: Topography, morphology and collateralization. *Brain Res. Bull.* **9**, 287–294 (1982).
45. L. Descarries, Y. Lapierre, Noradrenergic axon terminals in the cerebral cortex of rat. I. Radioautographic visualization after topical application of $_{DL}$-[^{3}H]norepinephrine. *Brain Res.* **51**, 141–160 (1973).
46. G. R. Poe, S. Foote, O. Eschenko, J. P. Johansen, S. Bouret, G. Aston-Jones, C. W. Harley, D. Manahan-Vaughan, D. Weinshenker, R. Valentino, C. Berridge, D. J. Chandler, B. Waterhouse, S. J. Sara, Locus coeruleus: A new look at the blue spot. *Nat. Rev. Neurosci.* **21**, 644–659 (2020).
47. V. Breton-Provencher, G. T. Drummond, J. Feng, Y. Li, M. Sur, Spatiotemporal dynamics of noradrenaline during learned behaviour. *Nature* **606**, 732–738 (2022).
48. M. E. Hasselmo, L. M. Giocomo, Cholinergic modulation of cortical function. *J. Mol. Neurosci.* **30**, 133–136 (2006).
49. M. Mather, D. Clewett, M. Sakaki, C. W. Harley, Norepinephrine ignites local hotspots of neuronal excitation: How arousal amplifies selectivity in perception and memory. *Behav. Brain Sci.* **39**, e200 (2016).
50. M. Sarter, C. Lustig, Forebrain cholinergic signaling: Wired and phasic, not tonic, and causing behavior. *J. Neurosci.* **40**, 712–719 (2020).
51. M. Sarter, V. Parikh, W. M. Howe, Phasic acetylcholine release and the volume transmission hypothesis: Time to move on. *Nat. Rev. Neurosci.* **10**, 383–390 (2009).
52. P. K. Zhu, W. S. Zheng, P. Zhang, M. Jing, P. M. Borden, F. Ali, K. Guo, J. Feng, J. S. Marvin, Y. Wang, J. Wan, L. Gan, A. C. Kwan, L. Lin, L. L. Looger, Y. Li, Y. Zhang, Nanoscopic visualization of restricted nonvolume cholinergic and monoaminergic transmission with genetically encoded sensors. *Nano Lett.* **20**, 4073–4083 (2020).
53. M. P. Kilgard, Cortical map reorganization enabled by nucleus basalis activity. *Science* **279**, 1714–1718 (1998).
54. R. C. Froemke, M. M. Merzenich, C. E. Schreiner, A synaptic memory trace for cortical receptive field plasticity. *Nature* **450**, 425–429 (2007).
55. A. R. Martins, R. C. Froemke, Coordinated forms of noradrenergic plasticity in the locus coeruleus and primary auditory cortex. *Nat. Neurosci.* **18**, 1483–1492 (2015).
56. M. Jing, Y. Li, J. Zeng, P. Huang, M. Skirzewski, O. Kljakic, W. Peng, T. Qian, K. Tan, J. Zou, S. Trinh, R. Wu, S. Zhang, S. Pan, S. A. Hires, M. Xu, H. Li, L. M. Saksida, V. F. Prado, T. J. Bussey, M. A. Prado, L. Chen, H. Cheng, Y. Li, An optimized acetylcholine sensor for monitoring in vivo cholinergic activity. *Nat. Methods* **17**, 1139–1146 (2020).
57. J. Feng, C. Zhang, J. E. Lischinsky, M. Jing, J. Zhou, H. Wang, Y. Zhang, A. Dong, Z. Wu, H. Wu, W. Chen, P. Zhang, J. Zou, S. A. Hires, J. J. Zhu, G. Cui, D. Lin, J. Du, Y. Li, A genetically encoded fluorescent sensor for rapid and specific in vivo detection of norepinephrine. *Neuron* **102**, 745–761.e8 (2019).
58. J. Feng, H. Dong, J. Lischinsky, J. Zhou, F. Deng, C. Zhuang, X. Miao, H. Wang, H. Xie, G. Cui, D. Lin, Y. Li, Monitoring norepinephrine release in vivo using next-generation GRAB$_{NE}$ sensors. *Neuron* **112**, 1930–1942.e6 (2023).
59. H. Wang, H. K. Ortega, H. Atilgan, C. E. Murphy, A. C. Kwan, Pupil correlates of decision variables in mice playing a competitive mixed-strategy game. *eNeuro* **9**, ENEURO.0457-21.2022 (2022).
60. D. J. Barraclough, M. L. Conroy, D. Lee, Prefrontal cortex and decision making in a mixed-strategy game. *Nat. Neurosci.* **7**, 404–410 (2004).
61. H. Seo, D. Lee, Temporal filtering of reward signals in the dorsal anterior cingulate cortex during a mixed-strategy game. *J. Neurosci.* **27**, 8366–8377 (2007).
62. A. Bernacchia, H. Seo, D. Lee, X.-J. Wang, A reservoir of time constants for memory traces in cortical neurons. *Nat. Neurosci.* **14**, 366–372 (2011).
63. D. G. Tervo, M. Proskurin, M. Manakov, M. Kabra, A. Vollmer, K. Branson, A. Y. Karpova, Behavioral variability through stochastic choice and its gating by anterior cingulate cortex. *Cell* **159**, 21–32 (2014).
64. H. Wang, A. C. Kwan, Competitive and cooperative games for probing the neural basis of social decision-making in animals. *Neurosci. Biobehav. Rev.* **149**, 105158 (2023).
65. D. Lee, Game theory and neural basis of social decision making. *Nat. Neurosci.* **11**, 404–409 (2008).
66. M. J. Siniscalchi, V. Phoumthipphavong, F. Ali, M. Lozano, A. C. Kwan, Fast and slow transitions in frontal ensemble activity during flexible sensorimotor behavior. *Nat. Neurosci.* **19**, 1234–1242 (2016).
67. F. Barthas, A. C. Kwan, Secondary motor cortex: Where 'sensory' meets 'motor' in the rodent frontal cortex. *Trends Neurosci.* **40**, 181–193 (2017).
68. J.-H. Yang, A. C. Kwan, Secondary motor cortex: Broadcasting and biasing animal's decisions through long-range circuits. *Int. Rev. Neurobiol.* **158**, 443–470 (2021).
69. M. Murakami, M. I. Vicente, G. M. Costa, Z. F. Mainen, Neural antecedents of self-initiated actions in secondary motor cortex. *Nat. Neurosci.* **17**, 1574–1582 (2014).
70. S. Pisupati, L. Chartarifsky-Lynn, A. Khanal, A. K. Churchland, Lapses in perceptual decisions reflect exploration. *Elife* **10**, e55490 (2021).
71. J. H. Sul, S. Jo, D. Lee, M. W. Jung, Role of rodent secondary motor cortex in value-based action selection. *Nat. Neurosci.* **14**, 1202–1208 (2011).
72. C. Maho, B. Hars, J.-M. Edeline, E. Hennevin, Conditioned changes in the basal forebrain: Relations with learning-induced cortical plasticity. *Psychobiology* **23**, 10–25 (1995).

73. B. Cusack, A. Nelson, E. Richelson, Binding of antidepressants to human brain receptors: Focus on newer generation compounds. *Psychopharmacology (Berl)* **114**, 559–565 (1994).
74. F. Ali, A. C. Kwan, Interpreting in vivo calcium signals from neuronal cell bodies, axons, and dendrites: A review. *Neurophotonics* **7**, 011402 (2020).
75. R. P. Tillage, N. R. Sciolino, N. W. Plummer, D. Lustberg, L. C. Liles, M. Hsiang, J. M. Powell, K. G. Smith, P. Jensen, D. Weinshenker, Elimination of galanin synthesis in noradrenergic neurons reduces galanin in select brain areas and promotes active coping behaviors. *Brain Struct. Funct.* **225**, 785–803 (2020).
76. L. Madisen, T. Mao, H. Koch, J. M. Zhuo, A. Berenyi, S. Fujisawa, Y. W. Hsu, A. J. Garcia III, X. Gu, S. Zanella, J. Kidney, H. Gu, Y. Mao, B. M. Hooks, E. S. Boyden, G. Buzsaki, J. M. Ramirez, A. R. Jones, K. Svoboda, X. Han, E. E. Turner, H. Zeng, A toolbox of Cre-dependent optogenetic transgenic mice for light-induced activation and silencing. *Nat. Neurosci.* **15**, 793–802 (2012).
77. J. Rossi, N. Balthasar, D. Olson, M. Scott, E. Berglund, C. E. Lee, M. J. Choi, D. Lauzon, B. B. Lowell, J. K. Elmquist, Melanocortin-4 receptors expressed by cholinergic neurons regulate energy balance and glucose homeostasis. *Cell Metab.* **13**, 195–204 (2011).
78. L. Swanson, B. Hartman, The central adrenergic system. An immunofluorescence study of the location of cell bodies and their efferent connections in the rat utilizing dopamine-B-hydroxylase as a marker. *J. Comp. Neurol.* **163**, 467–505 (1975).
79. P. Henny, B. E. Jones, Projections from basal forebrain to prefrontal cortex comprise cholinergic, GABAergic and glutamatergic inputs to pyramidal cells or interneurons. *Eur. J. Neurosci.* **27**, 654–670 (2008).
80. T. Patriarchi, A. Mohebi, J. Sun, A. Marley, R. Liang, C. Dong, K. Puhger, G. O. Mizuno, C. M. Davis, B. Wiltgen, M. von Zastrow, J. D. Berke, L. Tian, An expanded palette of dopamine sensors for multiplex imaging in vivo. *Nat. Methods* **17**, 1147–1155 (2020).
81. Y. Zhuo, B. Luo, X. Yi, H. Dong, X. Miao, J. Wan, J. T. Williams, M. G. Campbell, R. Cai, T. Qian, F. Li, S. J. Weber, L. Wang, B. Li, Y. Wei, G. Li, H. Wang, Y. Zheng, Y. Zhao, M. E. Wolf, Y. Zhu, M. Watabe-Uchida, Y. Li, Improved green and red GRAB sensors for monitoring dopaminergic activity in vivo. *Nat. Methods* **21**, 680–691 (2023).
82. Z. Kagiampaki, V. Rohner, C. Kiss, S. Curreli, A. Dieter, M. Wilhelm, M. Harada, S. N. Duss, J. Dernic, M. A. Bhat, X. Zhou, L. Ravotto, T. Ziebarth, L. M. Wasielewski, L. Sonmez, D. Benke, B. Weber, J. Bohacek, A. Reiner, J. S. Wiegert, T. Fellin, T. Patriarchi, Sensitive multicolor indicators for monitoring norepinephrine in vivo. *Nat. Methods* **20**, 1426–1436 (2023).
83. L. Beani, S. Tanganelli, T. Antonelli, C. Bianchi, Noradrenergic modulation of cortical acetylcholine release is both direct and gamma-aminobutyric acid-mediated. *J. Pharmacol. Exp. Ther.* **236**, 230–236 (1986).
84. G. Cuadra, K. Summers, E. Giacobini, Cholinesterase inhibitor effects on neurotransmitters in rat cortex in vivo. *J. Pharmacol. Exp. Ther.* **270**, 277–284 (1994).
85. W. Einhauser, C. Koch, O. L. Carter, Pupil dilation betrays the timing of decisions. *Front. Hum. Neurosci.* **4**, 18 (2010).
86. J. W. de Gee, T. Knapen, T. H. Donner, Decision-related pupil dilation reflects upcoming choice and individual bias. *Proc. Natl. Acad. Sci. U.S.A.* **111**, E618–E625 (2014).
87. J. C. Van Slooten, S. Jahfari, T. Knapen, J. Theeuwes, How pupil responses track value-based decision-making during and after reinforcement learning. *PLoS Comput. Biol.* **14**, e1006632 (2018).
88. J. Sturgill, P. Hegedus, S. Li, Q. Chevy, A. Siebels, M. Jing, Y. Li, B. Hangya, A. Kepecs, Basal forebrain-derived acetylcholine encodes valence-free reinforcement prediction error. bioRxiv 2020.02.17.953141 [Preprint] (2020). https://doi.org/10.1101/2020.02.17.953141.
89. J. H. Sul, H. Kim, N. Huh, D. Lee, M. W. Jung, Distinct roles of rodent orbitofrontal and medial prefrontal cortex in decision making. *Neuron* **66**, 449–460 (2010).
90. M. W. Howe, D. A. Dombeck, Rapid signalling in distinct dopaminergic axons during locomotion and reward. *Nature* **535**, 505–510 (2016).
91. M. Azcorra, Z. Gaertner, C. Davidson, Q. He, H. Kim, S. Nagappan, C. K. Hayes, C. Ramakrishnan, L. Fenno, Y. S. Kim, K. Deisseroth, R. Longnecker, R. Awatramani, D. A. Dombeck, Unique functional responses differentially map onto genetic subtypes of dopamine neurons. *Nat. Neurosci.* **26**, 1762–1774 (2023).
92. Z. Su, J. Y. Cohen, Two types of locus coeruleus norepinephrine neurons drive reinforcement learning. bioRxiv 2022.12.08.519670 (2022). https://doi.org/10.1101/2022.12.08.519670.
93. A. Uematsu, B. Z. Tan, E. A. Ycu, J. S. Cuevas, J. Koivumaa, F. Junyent, E. J. Kremer, I. B. Witten, K. Deisseroth, J. P. Johansen, Modular organization of the brainstem noradrenaline system coordinates opposing learning states. *Nat. Neurosci.* **20**, 1602–1611 (2017).
94. N. K. Totah, R. M. Neves, S. Panzeri, N. K. Logothetis, O. Eschenko, The locus coeruleus is a complex and differentiated neuromodulatory system. *Neuron* **99**, 1055–1068.e6 (2018).
95. T. Laszlovszky, D. Schlingloff, P. Hegedus, T. F. Freund, A. Gulyas, A. Kepecs, B. Hangya, Distinct synchronization, cortical coupling and behavioral function of two basal forebrain cholinergic neuron types. *Nat. Neurosci.* **23**, 992–1003 (2020).
96. N. Mechawar, C. Cozzari, L. Descarries, Cholinergic innervation in adult rat cerebral cortex: A quantitative immunocytochemical description. *J. Comp. Neurol.* **428**, 305–318 (2000).
97. K. L. Agster, C. A. Mejias-Aponte, B. D. Clark, B. D. Waterhouse, Evidence for a regional specificity in the density and distribution of noradrenergic varicosities in rat cortex. *J. Comp. Neurol.* **521**, 2195–2207 (2013).
98. S. E. Dougherty, T. J. Kajstura, Y. Jin, M. H. Chan-Cortes, A. Kota, D. J. Linden, Catecholaminergic axons in the neocortex of adult mice regrow following brain injury. *Exp. Neurol.* **323**, 113089 (2020).
99. S. Amemiya, A. D. Redish, Manipulating decisiveness in decision making: Effects of clonidine on hippocampal search strategies. *J. Neurosci.* **36**, 814–827 (2016).
100. C. I. Jahn, S. Gilardeau, C. Varazzani, B. Blain, J. Sallet, M. E. Walton, S. Bouret, Dual contributions of noradrenaline to behavioural flexibility and motivation. *Psychopharmacology (Berl)* **235**, 2687–2702 (2018).
101. G. A. Kane, E. M. Vazey, R. C. Wilson, A. Shenhav, N. D. Daw, G. Aston-Jones, J. D. Cohen, Increased locus coeruleus tonic activity causes disengagement from a patch-foraging task. *Cogn. Affect. Behav. Neurosci.* **17**, 1073–1083 (2017).
102. P. Vertechi, E. Lottem, D. Sarra, B. Godinho, I. Treves, T. Quendera, M. N. Oude Lohuis, Z. F. Mainen, Inference-based decisions in a hidden state foraging task: Differential contributions of prefrontal cortical areas. *Neuron* **106**, 166–176.e6 (2020).
103. T. E. Behrens, M. W. Woolrich, M. E. Walton, M. F. Rushworth, Learning the value of information in an uncertain world. *Nat. Neurosci.* **10**, 1214–1221 (2007).
104. M. van Holstein, S. B. Floresco, Dissociable roles for the ventral and dorsal medial prefrontal cortex in cue-guided risk/reward decision making. *Neuropsychopharmacology* **45**, 683–693 (2020).
105. C. K. Starkweather, S. J. Gershman, N. Uchida, The medial prefrontal cortex shapes dopamine reward prediction errors under state uncertainty. *Neuron* **98**, 616–629.e6 (2018).
106. H. Atilgan, C. E. Murphy, H. Wang, H. K. Ortega, L. Pinto, A. C. Kwan, Change point estimation by the mouse medial frontal cortex during probabilistic reward learning. bioRxiv 2022.05.26.493245 (2022). https://doi.org/10.1101/2022.05.26.493245.
107. D. G. R. Tervo, E. Kuleshova, M. Manakov, M. Proskurin, M. Karlsson, A. Lustig, R. Behnam, A. Y. Karpova, The anterior cingulate cortex directs exploration of alternative strategies. *Neuron* **109**, 1876–1887.e6 (2021).
108. S. Glaeser-Khan, N. K. Savalia, J. Cressy, J. Feng, Y. Li, A. C. Kwan, A. P. Kaye, Spatiotemporal organization of prefrontal norepinephrine influences neuronal activity. *eNeuro* **11**, ENEURO.0252-23.2024 (2024).
109. L. Pinto, K. Rajan, B. DePasquale, S. Y. Thiberge, D. W. Tank, C. D. Brody, Task-dependent changes in the large-scale dynamics and necessity of cortical regions. *Neuron* **104**, 810–824.e9 (2019).
110. M. J. Siniscalchi, H. Wang, A. C. Kwan, Enhanced population coding for rewarded choices in the medial frontal cortex of the mouse. *Cereb. Cortex* **29**, 4090–4106 (2019).
111. D. Lee, M. L. Conroy, B. P. McGreevy, D. J. Barraclough, Reinforcement learning and decision making in monkeys during a competitive game. *Brain Res. Cogn. Brain Res.* **22**, 45–58 (2004).
112. X. Wang, Z. Li, X. Wang, J. Chen, Z. Guo, B. Qiao, L. Qin, Effects of phasic activation of locus ceruleus on cortical neural activity and auditory discrimination behavior. *J. Neurosci.* **44**, e1296232024 (2024).
113. X. Fan, J. Song, C. Ma, Y. Lv, F. Wang, L. Ma, X. Liu, Noradrenergic signaling mediates cortical early tagging and storage of remote memory. *Nat. Commun.* **13**, 7623 (2022).
114. B. Yogesh, G. B. Keller, Cholinergic input to mouse visual cortex signals a movement state and acutely enhances layer 5 responsiveness. *eLife* **12**, RP89986 (2024).
115. A. Mathis, P. Mamidanna, K. M. Cury, T. Abe, V. N. Murthy, M. W. Mathis, M. Bethge, DeepLabCut: Markerless pose estimation of user-defined body parts with deep learning. *Nat. Neurosci.* **21**, 1281–1289 (2018).
116. T. Nath, A. Mathis, A. C. Chen, A. Patel, M. Bethge, M. W. Mathis, Using DeepLabCut for 3D markerless pose estimation across species and behaviors. *Nat. Protoc.* **14**, 2152–2176 (2019).
117. E. A. Pnevmatikakis, A. Giovannucci, NoRMCorre: An online algorithm for piecewise rigid motion correction of calcium imaging data. *J. Neurosci. Methods* **291**, 83–94 (2017).

Acknowledgments: We thank P. Jensen for generating and sharing the Dbh-Cre mice, N. Savalia for help with the two-photon microscope, and S. Thiberge, L. Pinto, and D. Tank for sharing the design of the laser steering system. **Funding:** This work was supported by the NIH/NIMH R01MH112750 (A.C.K.); NIH/NIMH R21MH118596 (A.C.K.); China Scholarship Council-Yale World Scholars Fellowship (H.W.); Gruber Science Fellowship (H.K.O.); NIH training grant T32NS007224 (H.K.O.); NIH/NIMH K08MH122733 (A.P.K.); NIH/NIMH R21MH134183 (A.P.K.); VA National Center for PTSD (A.P.K.); Brain and Behavior Research Foundation (A.P.K.); Cornell Engineering Learning Initiatives award (J.I.); and Cornell Institute of Biotechnology's Imaging Facility, supported by NIH 1S10RR025502 for the Zeiss LSM 710 confocal microscope. **Author contributions:** Conceptualization: H.W., H.K.O., and A.C.K. Methodology: H.W., H.K.O., J.I., and N.K.S. Investigation: H.W., H.K.O., E.B.K., J.I., and N.K.S.

Validation: H.W., H.K.O., E.B.K., J.I., and N.K.S. Formal analysis: H.W., H.K.O., N.K.S., and S.G-K. Visualization: H.W., H.K.O., and N.K.S. Resources: J.F. and Y.L. Supervision: A.P.K. and A.C.K. Funding acquisition: A.P.K. and A.C.K. Project administration: A.C.K. Data curation: H.W. and H.K.O. Writing—original draft: H.W., H.K.O., and A.C.K. Writing—review and editing: H.W., H.K.O., E.B.K., J.I., N.K.S., S.G.-K., A.P.K., and A.C.K. All authors reviewed the manuscript before submission. **Competing interests:** A.C.K. has been a scientific advisor or consultant for Empyrean Neuroscience, Freedom Biosciences, and Xylo Bio. A.C.K. has received research support from Intra-Cellular Therapies. A.P.K. received research funding from Freedom Biosciences and Transcend Therapeutics and has a patent application related to psychedelic treatments for PTSD. These duties had no influence on the content of this article. The authors declare that they have no other competing interests. **Data and materials availability:** All data needed to evaluate the conclusions in the paper are present in the paper and/or the Supplementary Materials. The data and code that support the findings of this study are available at Dryad: https://doi.org/10.5061/dryad.h44j0zpwk. The code is also available at https://github.com/Kwan-Lab/wangortega2025.

Submitted 24 July 2024
Accepted 20 February 2025
Published 26 March 2025
10.1126/sciadv.adr9916